https://doi.org/10.5194/egusphere-2026-2149
Preprint. Discussion started: 4 May 2026

Sediment transport capacity in a large braided river: integrating substrate mapping with flow scenarios

Justin M. Rogers[1], James Brasington[1], Jo Hoyle[2]

[1]Waterways Centre, School of Earth and Environment, University of Canterbury, Christchurch, 8140, New Zealand
[2]Earth Sciences New Zealand, Christchurch, 8011, New Zealand

Correspondence to: Justin M Rogers (Justin.Rogers@canterbury.ac.nz)

Abstract. Large braided rivers offer a challenging field environment and while our ability to map these complex environments through remote sensing has advanced significantly, even detailed surveys represent only a moment in time. In this study we have linked the remotely-sensed observations of substrate, including deposited fine sediment, at reach-scales to a hydraulic model of the braided Rangitata River, New Zealand. Excess fine sediment can alter fluvial form, ecosystem health and groundwater recharge. The advent of large-scale mapping technologies has enabled reconstruction of fluvial substrate facies over broad scales, and now spurs an examination of what can be learned with the greater fidelity of data from these surveys compared to simpler renditions of the riverbed. Here we propose a hybrid methodology that links spatially-distributed models of bed substrate with river hydraulics reconstructed from a ‘model library’ of steady state flows to better infer the controls on sediment transfer and deposition in braided rivers.

In this paper, we map potential sediment transport and depositional environments over a range of naturalised and modified flows. Our findings show that spatial bed data is the key to longitudinal consistency in sediment transport. The ‘model library’ method allowed us to efficiently test the tendency and magnitude of deficit, equilibrium, or surplus sand capacity in any location and the sensitivity of the result to bed composition, hiding and exposure formulations. The results indicate that the bed is sensitive to contemporary changes in hydrologic regime, particularly in the side channels accessible during the common ‘moderate’ flows that occur for tens of days per year. Simulations comparing the river’s sand transport capacity under the present hydrologic regime with a naturalised hydrologic regime indicate that the impacts of the flow abstractions are comparable to a 10-15% change in the bed sand fraction. Maps of potential sand deficit align well with observed depositional areas, and highlight the critical importance of the ‘moderate’ flows.

1. Introduction

1.1. Context and Aims

Braided rivers exhibit complex spatial and temporal variability in channel form and sedimentary processes, presenting persistent challenges for observing and modelling sediment transport dynamics (Ferguson, 2003; Parker, 2008). At any given hydraulic condition, potential sediment transport is influenced at the grain and patch scale by the local bed composition and morphology, which themselves reflect the integrated effect of flow and sediment supply. While considerable progress has been made in characterising topography and hydraulics, (Javernick et al., 2018; Schubert et al., 2015; Williams et al., 2014, 2015), the spatial and temporal variability of bed composition remains poorly constrained, despite its critical role in governing transport dynamics.

Fine sediment complicates sediment transport modelling by influencing the partitioning of bed shear stress, contributing to both bedload and suspended load. Despite its ecological significance, fine sediment is often excluded or oversimplified in gravel-bed transport formulations, with studies that fully integrate total sand with gravel transport dominated by flume or small river studies (Cui, 2007; Haddadchi and Rose, 2022; Le Minor et al., 2022). This gap reflects a broader challenge: the lack of spatially detailed, field-based data on grain size distributions (GSD) which inhibits our ability to parameterize transport models that are both physically meaningful and spatially explicit. Recent advances in data acquisition, from reach-scale bathymetric reconstructions to patch-scale GSD mapping, however, now offer new opportunities to better link substrate variability with the driving hydraulic forces at the scale of individual morphological units (Carbonneau et al., 2005; Ferguson et al., 2024; Marchetti et al., 2022; Williams et al., 2020; Woodget and Austrums, 2017). Detailed bathymetric mapping techniques now also allow observation of submerged bedforms, completing the reconstruction of channel form and roughness (Legleiter and Harrison, 2019; Williams et al., 2014).

In this study, we present a new modelling framework that combines high-resolution river morphology with spatially distributed observations of riverbed facies. Sediment transport of both gravel and sand is predicted by linking detailed substrate information to a library of steady-state, two-dimensional hydraulic predictions across a representative range of discharges. This approach allows reconstruction of spatially complex and time-varying flow fields across a range of hydrologic conditions. It does so in a computationally efficient way that supports sensitivity testing and transport scenario analysis without the overhead of fully unsteady simulations.

1.2. Gaps in flow and substrate coupling

Sediment transport in natural rivers is governed by interactions between hydraulics and bed structure across a continuum of spatial scales. At the grain scale, the packing geometry of individual particles and voids mediates transport through hiding and protrusion effects (Parker, 2008; Smith et al., 2023; Wilcock and Crowe, 2003). At the bar scale, local slope and 2D planform configuration govern local hydraulics and transport capacity. As channels diverge and converge in braided rivers, and as variation in sediment facies govern the local supply and entrainment potential of sediments, section- or width-averaged geometries are increasingly unable to capture the lateral and vertical complexity of flow and sediment motion (Ferguson, 2003). At the reach scale, the spatial arrangement of channel types reflects broader controls, including sediment supply, valley confinement, and hydrology.

In controlled laboratory settings, both hydraulics and bed composition can be precisely measured and manipulated. However, in the field, it is more feasible to measure, estimate, or solve for hydraulic conditions than to comprehensively characterise the properties of the substrate (e.g. grain size, sorting). Continual advances in spatially explicit numerical flow models have improved our ability to simulate fine-scale hydraulics, but computational demands remain constraining for detailed, large-scale and long-duration simulations (Javernick et al., 2018; Schubert et al., 2015; Williams et al., 2013). Alternatively, statistical approaches that abstract complex topography into generalised forms (Redolfi et al., 2016) have been used to predict transport, but these methods sacrifice spatial specificity and weaken the connection to field-based understanding of substrate and geomorphic processes.

Emerging observational methods are beginning to close this gap. Grain size statistics (e.g. D50) have been reliably retrieved over large river corridors using: optical and multispectral imagery (Buscombe et al., 2010; Carbonneau et al., 2005; Marchetti et al., 2022) and high-resolution microtopography from either photogrammetry or laser scanning (Ferguson et al., 2024; Hodge et al., 2009; Williams et al., 2020; Woodget and Austrums, 2017). Detailed bathymetric estimation techniques can now map channels at matching scales (Legleiter and Harrison, 2019; Williams et al., 2014), completing the terrain model and linking channel form and roughness.

Even with perfect stress partitioning, high-resolution hydraulics are insufficient without co-located information on bed composition. Here, we contend that a key remaining gap in sediment transport modelling is not hydraulics or even transport formulation, but in achieving equivalent detail and spatial coverage of the substrate.

1.3. Modelling Motivation and Objectives

A robust sediment transport model must match hydraulics with realistic representation of the bed structure. However, traditional 1D or quasi-2D models often rely on reach-averaged GSDs and simplified geometries, limiting their capacity to resolve key processes. When sediment transport occurs over beds with significant lateral and vertical heterogeneity in grain size, simplified models become ill-posed (Chavarrías et al., 2018). Fully morphodynamic models offer time-evolving resolution of processes at small spatial and temporal scales (Sun et al., 2015; Török et al., 2019; Williams et al., 2016), but remain computationally prohibitive for large braided systems.

In this study, we develop a 2D sediment capacity modelling framework that seeks to balance spatial complexity with computational efficiency. Specifically, we aim to:

- Capture local morphometric variability over large spatial scales;
- Integrate rich roughness and GSD estimates derived from large scale land cover classifications;
- Explore the sensitivity of transport predictions to the availability of these large datasets;
- Test the sensitivity of predictions to data gaps and hiding/exposure effects;
- Maintain longitudinal self-consistency in transport; and
- Compare the effects of different flow regimes (e.g. abstraction; event magnitude) on bedload and suspended sediment transport.

The approach is tested in application to a 56-km reach of the Rangitata River, New Zealand, where flow reduction due to abstraction may be causing adjustment in bed form or texture given an unchanged upstream sediment supply. Our modelling paradigm uses a library of steady-state simulations to transform arbitrary hydrologic time series into spatially explicit hydraulic predictions. These are then coupled to spatially detailed surficial substrate maps derived from remote sensing. By holding channel form constant, we sacrifice morphodynamic feedbacks but gain efficiency and clarity in assessing how a changed flow regime alters sediment transport capacity over space and time.

1.4. Fine Sediment

Excess fine sediment has been shown to degrade spawning habitat (Jowett and Boustead, 2001; Kemp et al., 2011); reduce the diversity of benthic invertebrates (Larsen et al., 2009; Matthaei et al., 2006); scour periphyton (Hoyle et al., 2017) and cause abrasion and clogging of fish gills (Kemp et al., 2011). More complex effects include fine substrate increasing the area on which vegetation can successfully grow, leading to a feedback loop where vegetation traps even more fine sediment (González del Tánago et al., 2015; Welber et al., 2012).

Despite these concerns, the representation of fine sediment in gravel-bed sediment transport formulae is often excluded. In part, this reflects the development of relationships through experimentation in controlled laboratory settings or simplified channels for reasons of scale and measurability. While the fine fraction is excluded in some formulae (Parker, 1990), in others it is used only as a modifier to the gravel transport rate (Curran and Wilcock, 2005; Wilcock and Crowe, 2003) or as part of a complete surface, subsurface and bedload-resolving model (Cui, 2007). Bimodal sand-cobble mixtures are rarely found in the gravel-bed literature, although many studies consider sand within bedload gravel transport models (Kuhnle, 1993; Williams et al., 2016) and a mixed bedload/suspended sand and bedload gravel transport method in a three-dimensional model showed promise at the reach scale (Török et al., 2020).

Research that focuses on the fine fraction amidst immobile larger clasts includes sand elevation approaches in flumes (Grams and Wilcock, 2014; Kuhnle et al., 2016; Raus et al., 2019; Trevisson and Eiff, 2022; Wren et al., 2014) and natural rivers (Haddadchi and Rose, 2022; Vericat et al., 2008). Both interstitial fines and fine sediment patches are important to storage and total transport, but the applicability of these studies at scale and over longer timeframes has not been tested. Multifraction sediment transport regimes in the sand-bed literature discuss hiding effects but do not cover the 10^3 ratio of grain sizes found in the study reach (van Rijn, 2007a).

Anecdotal reports of increasing fine sediment on the bed of the braided Rangitata River, NZ provides motivation to understand the processes controlling the distribution of sediment facies over a large braided river and the degree to which altered hydrology alters substrate. The lower Rangitata River has experienced flow reduction while the sediment supply from its upstream catchment remains naturally forced. Much of the literature regarding fine sediment in rivers focuses on dammed rivers starved of sediment, or increased fine sediment loading from factors such as land use change (González del Tánago et al., 2015; De Rego et al., 2020). The response of rivers to flow reduction can differ depending on the prior substrate; Gaeumann *et al.* (2005)

https://doi.org/10.5194/egusphere-2026-2149
Preprint. Discussion started: 4 May 2026

observed channel narrowing in a gravel reach and aggradation in a sand-bed reach of the Duchesne River. Similarly, reduction in geomorphically active flows in the lower Rio Grande resulted in channel narrowing and a positive feedback cycle between vegetation growth and vertical accretion of sediment that is only briefly reversed by channel-resetting floods (Dean and Schmidt, 2011).

1.5. Paper Structure

This paper first presents background and supporting data for the study site (Section 2). Section 3 provides a short review of the data products used in the paper, then describes the hydraulic and sediment transport modelling framework.

The results section is split into two parts. The first part (Section 4.1) describes the hydraulic performance of the flow model, using distributed field observations of depth and velocity and aerial imagery to interpret inundation area. Then, the behaviour of the model is demonstrated at representative points and reaches, and run through a series of sensitivity tests that vary the level of spatial complexity of the inputs to understand how our bed grain size maps constrain sediment transport, while also exploring the sensitivity to hiding and exposure parameters and assumptions regarding sampling gaps. The second part (Section 4.2) applies the most detailed application of the model to investigate longitudinal trends in sediment transport capacity in the Rangitata River under natural and modified flow regimes. Finally, Section 5 discusses the importance of spatial bed data, the ways we have considered fine sediment, the effects of altered hydrology, and the limitations and perspectives of the study.

2. Study Site

This modelling study leverages a unique dataset developed for the piedmont reach of the Rangitata | Rakitata River, Canterbury, New Zealand. This reach is defined as the lower 56 km of the river, which extends from below the bedrock gorge at the alpine mountain front to the sea. The upstream catchment is 1500 km² at the gorge, and this increases only marginally across the Canterbury Plains to 1773 km² at the coast. The reach has no major tributaries and rarely breaks out of its vegetated and engineered margins in events smaller than the decadal flood.

The reach can be divided into three geomorphic sections (see also Figure 1):

- **Upper 24 km**: Confined within terraces and vegetated margins;
- **Middle 23 km**: Laterally constrained by riparian vegetation and artificial training structures;
- **Lower 9 km**: Incised into the coastal plain.

Through this reach, the gradient decreases from 0.0065 to 0.004 and previous research suggests that the median grain size also decreases from 0.28 m to 0.04 m (Browne, 2004). These gradual changes in planform and sediment calibre create a quasi-experimental setting to investigate sediment transport dynamics.

The Rangitata is a rain-fed river, with the prevailing westerlies driving spill-over precipitation to the upper catchment over a 25-km watershed boundary on the W-E divide of the Southern Alps. A gauging station at the gorge, named Klondyke (#69302, -43.764462, 171.234798) has been maintained since 1934, with 5-minute flow data available since 1979. Daily data are

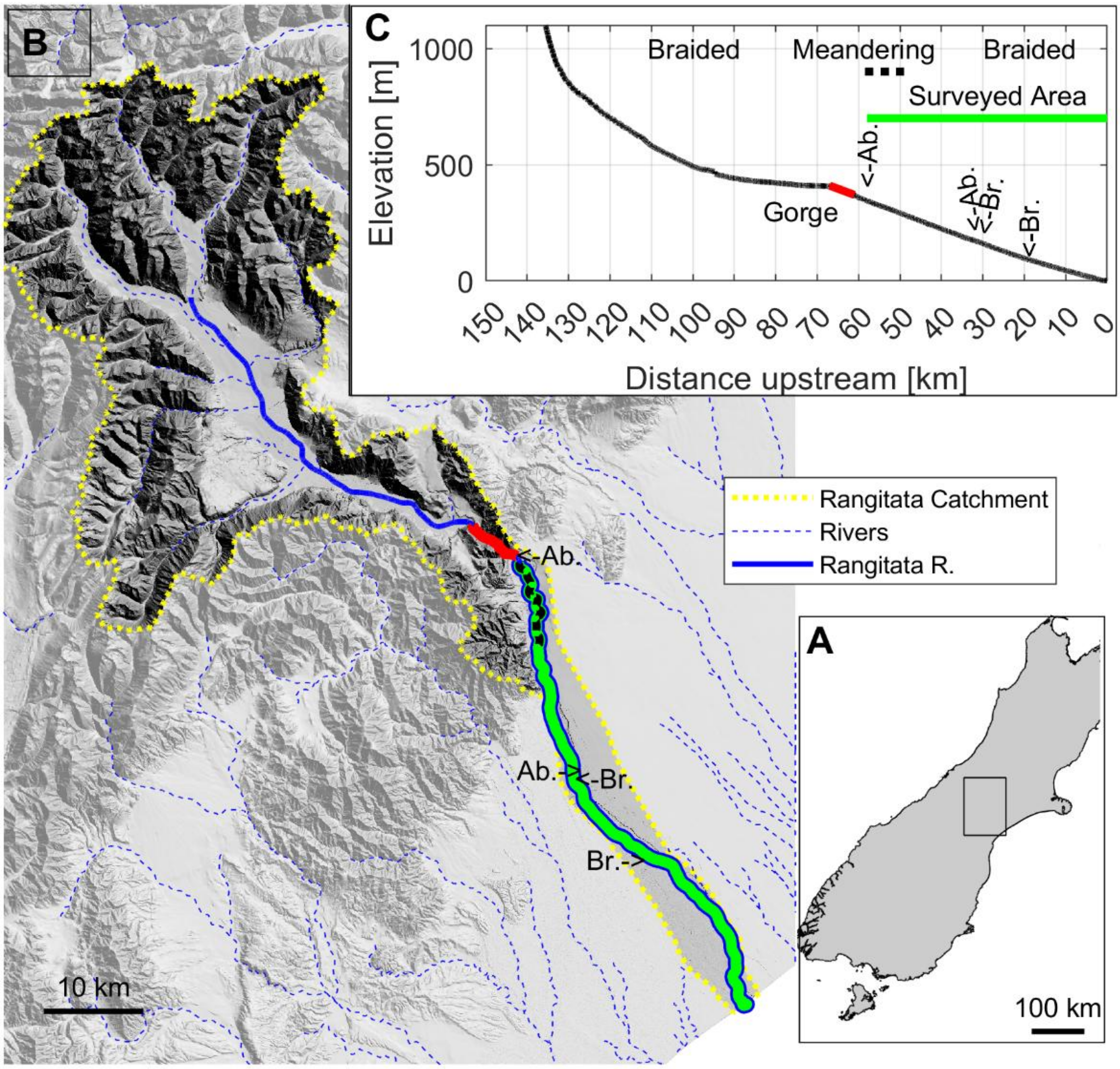

Figure 1 - The study area: A) Location map, South Island, NZ; B) Shaded relief map; C) Elevation profile of main stem, showing the surveyed reach and points of interest (water abstractions and bridges)

available from 1934. Based on the post-1979 record, the natural mean and median flow rates are 96.9 and 75.0 m^3/s respectively.

Two major abstractions (marked as "Ab." on Figure 1) modify the natural hydrology, taking water for irrigation and/or hydropower:

- Rangitata Diversion Race (RDR) at river km 56. Removes approximately 30% of the annual flow volume at intermediate and lower flows (Figure 2a,b). When flows exceed 140 m^3/s, the RDR intermittently flushes trapped fine sediment back to the mainstem (Figure 2d). Operating since 1945.
- Rangitata South (RS) at km 32. 'Harvests flood flows' above 110 m^{3}s^{-1}, removing 4.3% of the original flow volume. Sediment abstracted here may be permanently removed from the river (Fig. 2d). Operating since 2011.

A typical event hydrograph illustrates how the abstractions reduce the residual flow (Fig. 2a), while their effect on the flow duration record is shown in Fig. 2b. Post-abstraction, the mean and median flow rates fall to 63.6 m^3/s and 67.8 m^3/s respectively. This diminution of intermediate-sized flows, along with the periodic flushing of trapped sediment, has led to concerns over the build-up of surficial and interstitial fine sediment.

Flow duration analysis reveals c. 12 events annually exceed 225 m^3/s (3x median flow); 70% of these occur in the austral summer, between October - March. The annual Richards–Baker flashiness index (Baker et al., 2004) increases from 0.4 (σ = 0.08) for the natural hydrograph, to 0.61 (σ = 0.10) below the RDR and 0.60 (σ = 0.11) below RS after abstraction. This is relatively high for the catchment size (Baker et al., 2004) and underpins the importance of analysing transport dynamics across a range of events, not just a mean annual flood.

A historical suspended sediment dataset from the gorge, combined with recent turbidity measurements from February to June 2020 at the upper abstraction, was used to develop a sediment rating curve (Fig. 2c). The best fit is achieved using two bias-corrected power law regressions, based on the RiverLoad method (Ferguson, 1986; Nava *et al.*, 2019), with a hinge point at around 160 m^{3}s^{-1}.

The turbidity record reflects sand, silt- and clay-sized suspended sediment (Bright et al., 2020). Recent observations (Haddadchi and Measures, 2025) reported sand fractions of between 39% and 50% in two moderate events (peaking at 183 and 164 m^3/s respectively) and 27% during a larger flood. Hysteresis patterns in the short flow - turbidity record show inconsistent phasing and the drivers of changes in sediment composition during events remains unclear. Given these uncertainties, we adopt a representative sand fraction of 40% for the suspended sand load likely to interact with the bed. The silt and clay wash load are not considered further.

https://doi.org/10.5194/egusphere-2026-2149
Preprint. Discussion started: 4 May 2026

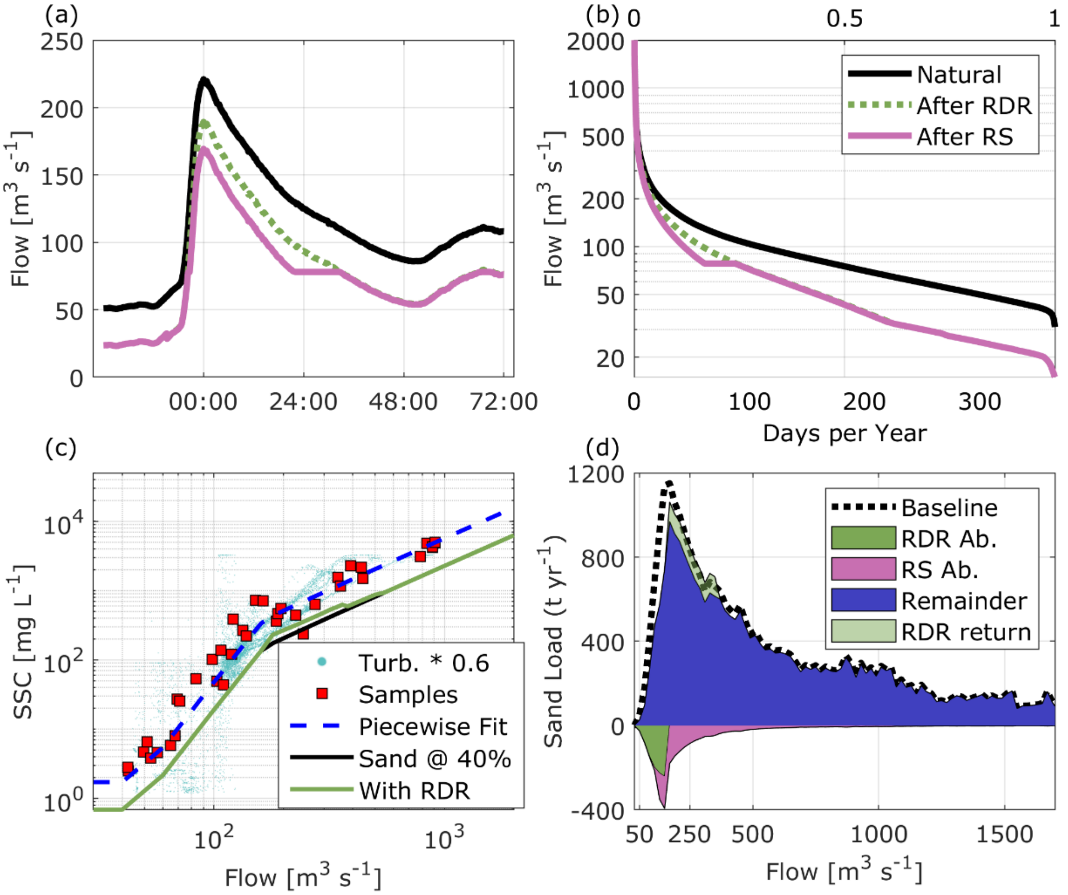

Figure 2 - (a) example event flow timeseries, (b) Flow frequency curves (c) Suspended sediment rating curve (d) Suspended sand load vs discharge. Combining flow frequency (b) and sediment rating curves (c) produces the load curve (d), expressed per 1 m^{3}s^{-1} bin. Abstractions are represented as a negative load, while the flushing of the RDR sand trap adds the same material back to the river at higher flows.

The sediment load curve (Figure 2d) reveals that a negative sand load below 140 m^3/s is offset by a positive load between 140 and 350 (est.) m^{3}s^{-1}. The RS abstraction is assumed to permanently remove its sand load to off-channel storage ponds. Examination of the load curve also highlights the dominant role of frequent, moderate flows (100-500 m^{3}s^{-1}) in transporting the suspended sediment load, as implied in the classic analysis of Wolman and Miller (1960). By shifting sand transport from low to intermediate flows, abstraction and flushing may redirect sand deposition from the core channel network to higher elevations, secondary channels and backwaters. Further abstractions may also limit the reworking necessary to clear interstitial sand. Hicks *et al*. (2011) estimated annual suspended load as 1.5760 Mt/yr; applying our 40% sand fraction assumption yields an annual sand load of ~630 kt/yr. We model sand with a D50 of 250 μm and neglect the silt and clay fractions. Bedload upstream of the gorge was estimated at between 42 and 138 kt/yr (Healey, 1997). At the coast, Gibb and Adams (1982) suggest this flux rises to ~281 kt/yr, a value that is approximately half of the estimated postglacial excavation rate of 580 kt/yr (Adams, 1980)

3. Methods

3.1. Geospatial Surveys and Data Acquisition

Accurate, spatially explicit estimates of sediment transport require high-resolution topographic, bathymetric and bed composition data. To support this, a lidar and RGB aerial survey was conducted over the lower 56 km of the Rangitata River in March 2021 (Figures 1, 3a). This survey generated a dense 3D point cloud (80-100 pts/m^2) and co-registered orthoimagery with a ground resolution of 0.025 m. The point cloud was classified into ground and off-ground points using Terrasolid and a 1 m digital elevation model (DEM) was interpolated. A RGB orthomosaic was constructed by aerotriangulation using ArcGIS Pro. Full details of the acquisition and modelling are presented in Rogers *et al*., (2025). Multiple rasters were derived from the lidar and RGB data to support machine learning classification of bed facies at 1 m resolution. These raster predictors include colour and lidar intensity (mean and standard deviation), point dimensionality, and surface elevation statistics (Brasington et al., 2012; Brodu and Lague, 2012; Weidner et al., 2021).

A longitudinal survey of bathymetry and flow velocity was undertaken to provide synoptic observations to calibrate water depth from reflectance values in the aerial photography. A Sontek M9 aDcp with integrated GNSS was towed along a c. 25 km reach following the principal channel thalweg. Quality control included checks on bottom-track signal validity, presence of multiple vertical bins, consistency between measured velocity and GPS speed-over-ground, and consistency between vertical beam and four-beam depth to remove data spikes. These measurements were used to build a bathymetry-from-colour regression model to create a continuous DEM, following the approach of Williams *et al.* (2014). Velocity data were depth-averaged and retained for model validation. Flow gauging by Environment Canterbury staff on the survey day recorded a natural flow at the gauged transect of 53.6 m^3/s that matched closely the Klondyke gauge reading of 54.4 +/- 0.4 m^3/s. The consented abstraction at this flow is 27.1 m^3/s, leaving 26.5 m^3/s assuming the consented amount was taken. Five gauging transects spaced throughout the lower 56 km averaged 26.0 +/- 1.7 m^3/s, with the river mouth approximately 2 m^3/s lower than the post-abstraction flow.

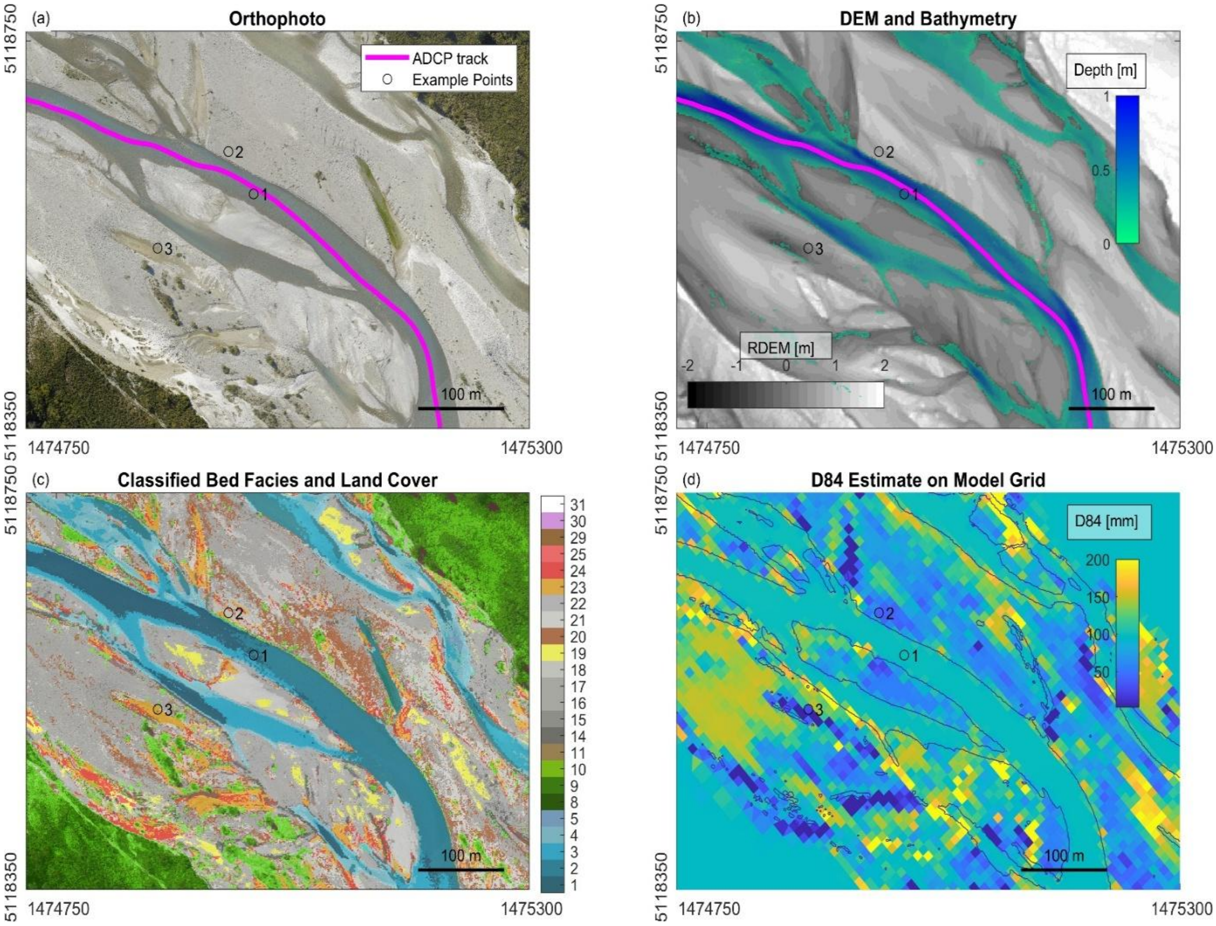

Figure 3 - (a) Orthoimage from March 21, 2021 lidar+RGB survey with aDcp track; (b) DEM relative to mean water level and depth estimate from colour estimator; (c) Classified river facies map, with gravels in greyscale and fine sediment in orange/red, and (d) Estimate of bed material D84 from spatial GSD map. Numbered points are exemplars for the thalweg, edge of major channel, and dry braided channel locations, as referred to in Figure 7.

Classification of the riverbed into representative sediment facies followed the method of Rogers *et al.* (2025). The approach effectively distinguished areas of fine sediment as well as common bimodal cobble and fine material facies. Coarser substrates were further subdivided into gravel, gravel-cobble, cobble, and cobble-boulder facies, based primarily on surface roughness.

https://doi.org/10.5194/egusphere-2026-2149
Preprint. Discussion started: 4 May 2026

These facies were transformed into quantitative grain size distributions (GSDs) and sand fractions on a 1 m² raster. The dominant braidplain facies were validated using pebble counts, while some less common classes were attributed GSDs by class interpolation (Figure 4a). Vegetated areas were assigned the river-wide median GSD.

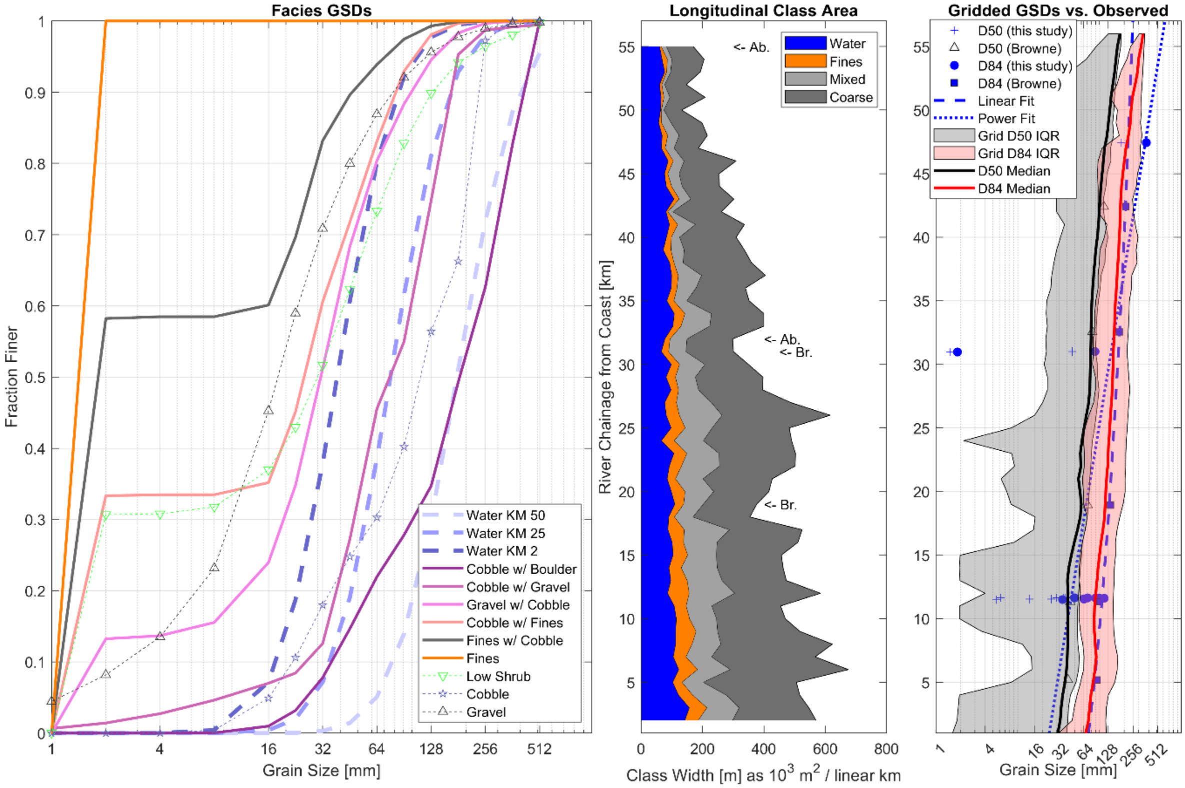

Figure 4 – (a) Training patch (solid lines) and synthetic (dashed lines) GSDs, (b) Longitudinal sediment facies prevalence expressed a width and (c) Median (solid line) and interquartile range (shaded) of predicted D50 and D84 grid points (shaded). Fitted curves to observed D50 and D84 (dashed) are used to fill data gaps in submerged areas. See Figures S1 – S4 for additional GSD comparisons for the Ealing reach, KMs 9-12.

Grain size distributions for areas submerged during the lidar survey were estimated using a piecewise fit to observed gravel D50 and D84 Wolman data from this study, along with counts from (Browne, 2004; Measures, 2013), as shown in Figure 4c. The fit captures the steep downstream fining associated with the transition from upstream confined meandering reaches to lower braided reaches, using a linear fit through the braided section and a power law upstream of KM 36 to separate the two morphologies. The true bed GSDs are highly variable and approximated here by applying the same longitudinal GSD to all wetted channel areas in a cross-section.

Aggregation of the pixel-based data onto the hydrodynamic grid first used a decomposition method based on Chapuis (2023) to fit exemplar GSDs for each facies, which were assigned to each classified 1 m² cell. The GSDs within each hydrodynamic grid cell (50-90 m²) were then averaged on the cumulative distribution function to produce a single GSD per grid cell. This approach preserved bimodal sand-cobble facies while simplifying the 10^{10} m² of riverbed into ~3 x 10^3 grid cells. Figure 4b shows the longitudinal distribution of facies, with uniform sand facies increasing toward the coast. Bimodal cobble–sand facies are labelled 'mixed,' and coarse, low-sand materials are distributed throughout the river.

The resulting gridded D50 and D84 values generally follow the observed longitudinal trends, except in the uppermost reaches, where a single 'Cobble-Boulder' class proved too coarse to capture the variability. We also note that finer material remains present in some coarse facies, particularly in backwaters and disconnected channels, and in the subsurface which we do not resolve. These uncertainties are addressed in sensitivity tests. Across the wetted braidplain, the global median D50 is very close to 0.050 m. For comparative purposes, simplified GSDs with D50 of 0.025, 0.050 and 0.100 m and $\sigma = 1\varphi$ were constructed for testing against our spatially variable GSDs. The gridded D50 and fine sediment fraction data were also compared statistically with a larger set of bed material pebble count data, and two subsurface bulk samples, in the co-located reach, collected in the prior two years by ESNZ (see supplementary figures S1-4).

3.2. Model Framework and Design

Here we present a new framework for modelling sediment transport capacity that integrates spatially explicit substrate information with a computationally efficient hydraulics framework. Spatially distributed hydrodynamic variables - depth, velocity, shear stress - are reconstructed from a precomputed library of steady-state model outputs, each corresponding to a specific discharge. This enables the approximation of local, time-varying hydraulic conditions for an arbitrary timeseries of flows without the computational burden of continuous unsteady simulation.

Sediment transport capacity is calculated for each model grid cell and for each discharge and then aggregated to reach-scale summaries and interpolated in time. The model framework is presented diagrammatically in Figure 5 and the transport equations described below in Section 3.4, with particular focus on the key spatial inputs: depth, velocity, and grain size distribution (GSD). Parameters with spatial variability are emphasised in **bold** text in the equations.

While the steady-state assumption neglects storage dynamics and hysteresis effects, it allows the spatially explicit flow features to be resolved. These include backwaters, eddies, and secondary circulation which are parameterised through the underlying

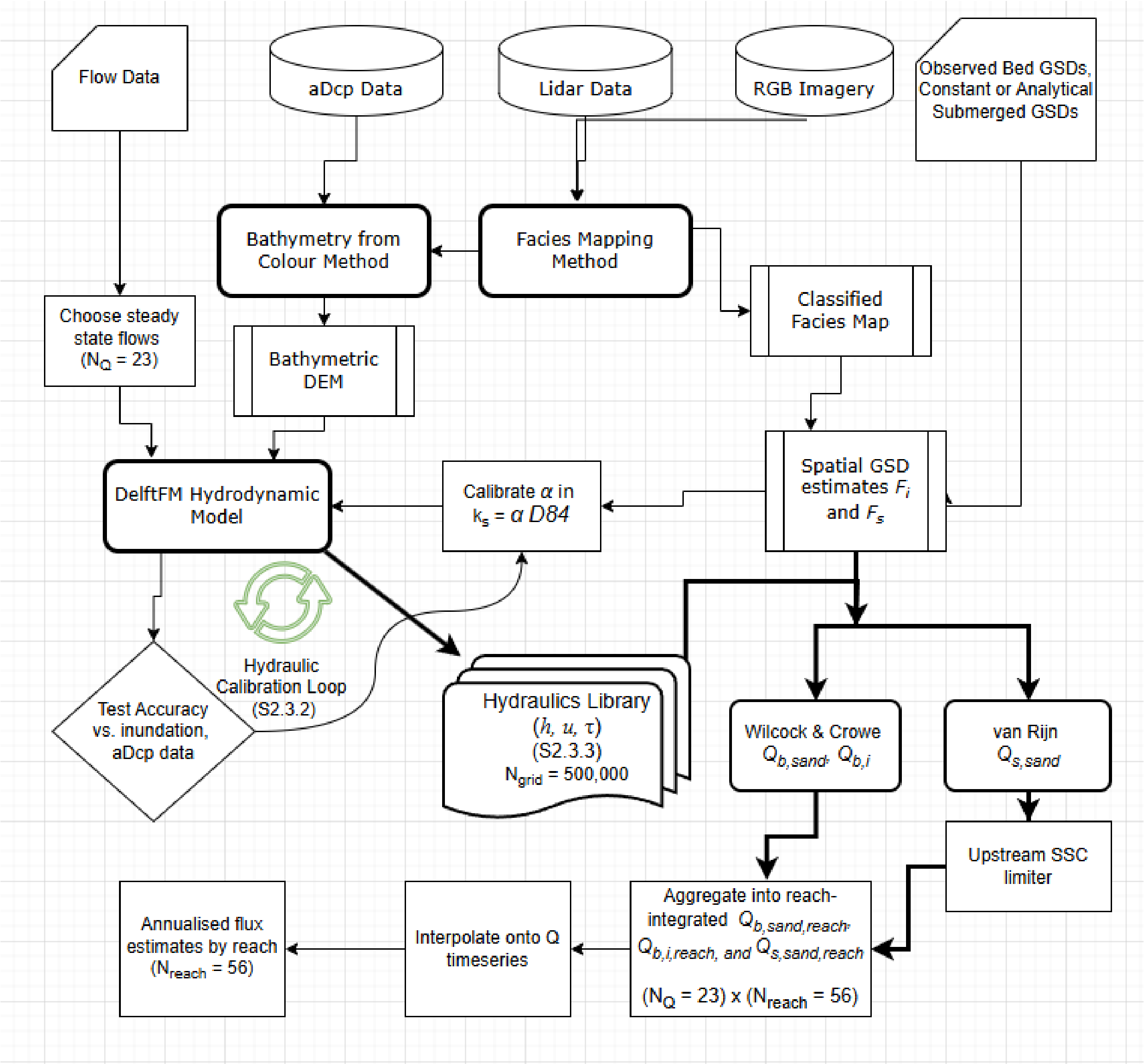

Figure 5 - Transport capacity modelling method flowchart.

2D hydraulic model and governed by the local channel morphology. The method makes a vastly simplifying assumption that the only temporal variability is flow, driving hydraulics, and the bed does not evolve during or between flow events.

3.2.1. Numerical Model

The hydrodynamic grid and simulations were developed using the 2D numerical model Delft Flexible Mesh (Deltares, 2021). Initial discretization used a valley-following curvilinear grid of 32-40 m resolution. This grid was then refined iteratively by simulating steady state flow at the mean annual flood discharge. The inundated extent from each run was used to progressively refine the grid, converging on a final resolution of 7-8 m in active areas. This resolution aligns with the smallest scale tested in Schubert (2015) and follows their guidance on automatic grid generation at large scales.

Stecca *et al*. (2022) found that a 9 m horizontal resolution grid was too coarse for capturing the morphological evolution of small-scale fluvial features but still reproduced realistic channel width and braiding intensity. This suggests that channel-scale hydraulics were well resolved in our model. Altenau *et al.* (2017) also showed that large river models (>90 km) at similar resolution have water surface elevation (WSE) uncertainties comparable to traditionally surveyed data. They noted, however, significant bathymetric uncertainty at this scale and recommended further research into the parameterization of roughness in large multi-threaded rivers.

The topographic and bathymetric DEMs were interpolated onto the model grid. Spatially varying bed roughness was parameterised using the White-Colebrook formulation:

$$C_{2D} = \frac{\sqrt{g}}{\kappa}\log\left(1+\frac{30\mathbf{h}}{e k_s}\right) \qquad (1)$$

where $k_s = \alpha \boldsymbol{D}_{\mathbf{84}}$, $\mathbf{h}$ is depth, e is Euler's number, κ is the von Kármán constant, and g is gravitational acceleration.. The value of D84 was estimated for each grid cell based on its GSD and the roughness scaling parameter α was tested and calibrated against aDcp and inundation observations (Section 4.1.1). Vegetation roughness parameterisation from land cover was tested (Abu-Aly et al., 2014) but found to be inconsequential at all but the highest flows. The downstream boundary was forced with an idealised time series of predicted tide heights, used only to exclude the reach subject to tidal influence.

3.3. Flow Scenarios

Running high-resolution models over large spatial domains is computationally intensive, rendering long-term unsteady simulations impractical. To address this, our flow library approach produced a look-up table of predicted hydraulic variables – depth (h), velocity (u) and shear stress (t) – for each grid cell across a range of discharges.

The hydrograph was discretized into n = 23 representative flow conditions, selected by percentile from timeseries with and without known abstractions. Each flow scenario was then run as a steady-state simulation, with the model forced at the upstream boundary with a constant discharge until the flow field reached equilibrium, confirmed by matching inflow and outflow. Although large floods are rarely in steady state over large reaches (Bales and Wagner, 2009), a flow library approach enables efficient approximation of key hydraulic variables for any time series of flows. Linear interpolation between steady-state solutions allows reconstruction of time-varying hydraulics without the computational burden of solving the full dynamic flow equations. The flow library method was tested against a time-stepping event simulation by re-interpolating the steady state results onto the event simulation and comparing depth, velocity and shear stress.

3.4. Sediment Transport Calculations

To make optimal use of the rich information on the spatial variability in bed composition, transport capacity must be calculated at high spatial resolution. However, simulating morphologic change would immediately invalidate the fixed substrate map. Therefore, here we estimate transport capacity, not actual transport, and do not simulate changes in sediment concentration over time or space.

The precomputed library of 2D steady-state hydraulic results was transformed into sediment transport capacity estimates using a post-processing approach in Matlab. These include both bedload and suspended sand components. For each discharge scenario, transport was calculated at the grid-cell scale, then aggregated into a width-integrated transport rate for each analysis reach.

Bedload

Gravel and sand bedload transport is calculated using the Wilcock and Crowe (2003) formulation ("WC" hereafter), parameterized with the surface grain size distribution. The dimensional sand bedload transport rate at each grid cell is given by:

$$qb_{WC} = W_i^* \cdot \boldsymbol{F_s} \cdot \frac{\boldsymbol{u_*^3}}{sg} \tag{2}$$

where: F_s is the local sand fraction; s the ratio of sediment to water density; g is the acceleration due to gravity; $\mathbf{u}_*$ is the shear velocity; and W_i^* the dimensionless transport rate:

$$W_i^* = \begin{cases} 0.002 \cdot \phi^{7.5} & , \phi < 1.35 \\ 14\left(1 - \frac{0.894}{\sqrt{\phi}}\right)^{4.5} & , \phi \geq 1.35 \end{cases} \tag{3}$$

where $\phi = \tau / \tau_{ri}$ is the ratio of the shear stress at each grid cell to the grain-specific reference shear stress.

Hiding effects are incorporated based on the ratio of the specific grain size D_i to the mixture median grain size D_{50}:

$$\tau_{ri} = \tau_{rs50}\left(\frac{D_i}{\boldsymbol{D_{50}}}\right)^b \tag{4}$$

with the reference shear stress of the mixture represented by the D_{50} and modified by the bed sand fraction:

$$\tau_{rs50} = \left(0.021 + 0.015 \cdot e^{-20 \cdot \max(0.01, \boldsymbol{Fs})}\right) \cdot g \cdot \boldsymbol{D_{50}} \cdot \rho_w \cdot (s - 1) \tag{5}$$

and the hiding exponent b given by:

$$b = \frac{0.67}{1 + e^{(1.5 - D_i/\boldsymbol{D_{50}})}} \tag{6}$$

Gravel bedload transport is calculated using the same formulation, substituting the gravel fraction $\boldsymbol{F_i}$ for $\boldsymbol{F_s}$ in Equation 2.

Suspended Sand

Suspended sand transport is influenced by the presence of coarse substrate and the distinction between bedload and suspended load can be ambiguous (Wainwright et al., 2015). In this study, the suspended sand transport capacity is estimated using the approach of van Rijn (2007a) with key parameters adapted from the gravel-sand experiments of Kleinhans and van Rijn (2002) ("VR" hereafter).

The suspended sediment flux per unit width, q_s, is estimated using a reference concentration, c_a, modified by a shape factor F that accounts for the vertical distribution of concentration.

$$c_a = 0.015 \frac{D_i}{a_{VR}} \cdot \frac{T^{1.5}}{D_*^{0.3}}) \qquad (7)$$

Where: D_i is the local sand grain size (assumed here to be 250 µm); a_{VR} is the reference elevation defined as $2 \cdot \boldsymbol{D_{50}}$, T is the transport stage parameter; and D_* is the dimensionless grain size.

The total suspended sediment flux is then calculated as:

$$qs_{VR} = \boldsymbol{u}\,\boldsymbol{h}\, min(F\, c_a\, \boldsymbol{F_s}\ , SSC_{Gorge}) \qquad (8)$$

Where: u is the local velocity; h is flow depth; F_s is the local sand fraction; and SSC_{Gorge} is the supply-limited concentration based on the upstream sediment rating curve. The factor F is a shape factor accounting for the suspended concentration profiles, damping and hindered settling (Deltares, 2021; van Rijn, 2007b). This formulation ensures that suspended sand transport is constrained by both local hydraulics and the available sediment supply.

Constraints on the Transport Stage Parameter

The suspended transport stage parameter, T, is constrained by three factors. First, a grain size ratio hiding factor, γ_{McC} , based on the function of McCarron (2019). This accounts for reduced transport efficiency when fine sand is embedded within coarser substrates (Kleinhans and van Rijn, 2002). Second, the bed sand fraction, Fs, is used to represent the local availability of sand for suspension. Third, transport is capped by the incoming, upstream, suspended sediment concentration, represented by the sediment concentration at the gorge (SSC_{Gorge}).

The hiding factor, γ_{McC}, is calculated as:

$$\gamma_{McC} = \gamma_{sand} + \left(\gamma_{grav} - \gamma_{sand}\right)(1 - \boldsymbol{Fs})^{1.73} \qquad (9)$$

The hiding correction for each grain size is then:

$$\xi_i = \left(\frac{D_i}{\boldsymbol{D_{50}}}\right)^{-\gamma_{McC}} \qquad (10)$$

$$\xi = \min(\xi, \xi_{max}) \qquad (11)$$

To avoid extreme hiding effects when sand coexists with coarse substrates, ξ_{max} is tested over a range from 1 (no hiding) to 40. The upper bound reflects the $1{:}10^3$ grain size ratio between sand and cobble, which lies beyond the range tested in previous studies.

Calculation of Transport Stage, T

The transport stage parameter T is calculated as the ratio of excess grain-related shear stress to the critical shear stress for sand motion (here assumed to be 250 µm):

$$T = \frac{\tau' - \xi_i \, \tau_{cr,i}}{\tau_{cr,i}} \tag{12}$$

Where: τ' is the grain-related bed shear stress; and $\tau_{cr,i}$ is the critical shear stress for sand. The grain related shear stress is estimated using:

$$\tau' = \rho g (\mathbf{u}/C')^2 \tag{13}$$

$$C' = 18 \log_{10} \frac{12\,\boldsymbol{h}}{k_{s,grains}} \tag{14}$$

The critical shear stress for 250 µm sand is calculated as:

$$\tau_{cr} = (\rho_s - \rho_w) g \boldsymbol{D_{sand}} \theta_{cr} \tag{15}$$

$$\theta_{cr} = 0.15\, D_*^{-0.64} \tag{16}$$

Where the dimensionless grain size is:

$$D_* = D_{sand}\, ((s-1)\, g \,/\, \upsilon^2)^{1/3} \tag{17}$$

Where: s is the water to sediment density ratio ρ_s/ρ_w and is υ kinematic viscosity.

This approach follows the partitioning method of Kleinhans and van Rijn (2002), where grain-related shear stress is estimated from the modelled depth and velocity. A constant grain roughness length $k_{s,grains} = 10 * D_{sand}$ is used due to insufficient data on the behaviour of sand within a cobble or gravel matrix. A constant based on the sand size is chosen here as we are varying many other GSD-dependent parameters in our model.

Grams and Wilcock (2007, 2014) provide one of the few studies on the behaviour of sand transport amongst immobile cobble beds. They showed that sand transport rates are a combination of high mobility in sand patches and lower mobility in interstitial sands. Total transport is parameterised in terms of a relative sand elevation z_s, which reflects the vertical position of sand relative to the surrounding coarse framework. Their results suggest that sand entrainment is greater than predicted by hiding-based formulations, since above a certain sand elevation increased turbulence from coarse elements on the bed enhances the likelihood of interstitial sand being entrained. To test the sensitivity of our approach to this behaviour, we implemented the Grams and Wilcock (2014) formulation (GW14) in post-processing by substituting an effective sand availability $F_{s,GW}$ in place of F_s in the suspended transport formulae above. The modified availability if defined as:

$$F_{s,GW} = \left(1 + e^{-9.3(z_s - 0.13)}\right)^{-2.8} \tag{18}$$

Where the relative sand elevation is taken to be

$$z_s = 0.25 - 0.25 \ln(\boldsymbol{F_s}^{1/5} - 1) \tag{19}$$

inverted from Equation 8 of Grams and Wilcock (2007). This formulation accounts for the nonlinear increase in sand transport capacity as sand patches build up above the coarse framework. It provides a more physically based alternative to hiding corrections when fine sediment is embedded within rough riverbeds.

3.5. Post-Processing

Gridded estimates of bedload and suspended sand transport were aggregated over 56 non-overlapping reach polygons that segment the river corridor into 1 km downstream cells. The irregular shape of the flexible mesh grid and the reach polygons complicates typical cross-section calculations. To address this, we adopt a reach-based aggregation method that uses the ratio between the known steady-state discharge and the sum of each model cell's discharge to enforce consistency using a closure factor. For each cell, discharge of water is estimated as:

$$Q_w = \boldsymbol{u} * \boldsymbol{h} * b' \qquad (20)$$

Where, u is depth-averaged flow velocity, h is flow depth and b' is the representative grid cell width in the valley-parallel direction. The total modelled discharge is then summed and compared to the known input discharge, allowing the calculation of a discharge closure factor, Q_{corr}:

$$Q_{\mathrm{corr}} = \frac{\sum Q_w}{Q_{\mathrm{known}}} \qquad (21)$$

Where Q_{known} is the steady discharge at the upstream boundary. This discharge closure factor is then used to normalize the aggregated sediment transport rates within each reach. The reach-aggregated transport rates for both suspended and bedload sand are given as:

$$Q_{s,\mathrm{Reach}}(KM, Q) = \frac{\sum(Q_s * b\prime)}{Q_{\mathrm{corr}}} \quad , \; Q_{b,\mathrm{Reach}}(G, Q) = \frac{\sum(Q_b * b\prime)}{Q_{\mathrm{corr}}} \qquad (22)$$

These normalized values, $Q_{s,\mathrm{Reach}}$ and $Q_{b,\mathrm{Reach}}$, can be interpolated onto any flow or value of or flow timeseries. The approach was verified by comparing single cross-section integrations of Q_s, but it must be noted that the method only applies to sediment transport capacity when using our static-bed assumptions. This enables visualization of transport capacity as a function of discharge (e.g., as histograms or rating curves) or transformation in annual loads (tons per year) for comparison across reaches and between hydrologic scenarios. In summary, this approach enables rapid testing of multiple sediment transport assumptions by post-processing the stepped discharge library.

4. Results

4.1. Model testing, demonstration and sensitivity

The results are structured in two parts. Section 4.1 compares the hydraulic predictions against observations, then poses a series of sediment transport sensitivity tests designed to assess the robustness of the modelling framework and the value of spatially distributed data inputs. Section 4.2 applies the model to the Rangitata River, using the spatially distributed transport capacity estimates to characterise longitudinal trends, evaluate hydrologic controls, and assess the geomorphic implications of altered flow regimes.

4.1.1. Model testing, demonstration and sensitivity

Method

The flow model was calibrated by varying the α parameter, which estimates grain roughness k_s from the spatial D84 data (Eqn. 1). The modelled flow fields were tested against low-flow inundation extent from the classified lidar/RGB survey and aDcP data in the channel thalweg. We follow the approach of Williams *et al.* (2013), using ratio of modelled and observed wetted width $FitW_E$ and the spatially explicit fit $Fit_{Congruent}$. Depth and velocity are compared to the aDcp data at collocated model cells with the skill metric of Willmott (1981):

$$Skill = 1 - \frac{\sum_{i=1}^{n}(P_i - O_i)^2}{\sum_{i=1}^{n}(|P_i - \overline{O}| + |O_i - \overline{O}|)^2} \tag{23}$$

with P the prediction and O the observation, as well as RMS error and bias metrics. Water level data collected years after the lidar survey allowed a qualitative understanding of modelled vs observed celerity over a 36-km distance, but the channel configurations did not match so these are not relied upon.

Interpolation from the flow library was tested against time-stepping event simulations using (i) a comparison of depth and velocity timeseries at specific points, and (ii) a global comparison of event-integrated shear stress. The time series from a single event was compared to the flow library interpolated time series over the same time period. The event-integrated shear stress metric avoids the temporal mismatch between interpolated and event flows, focusing on the total force available for sediment transport.

Hydraulic model performance

The best-performing models in terms of inundation, depth and velocity had α between 0.2 and 0.4, which are within the lowest few outliers in the review of López and Barragán (2008). Our site has low relative submergence and complex morphology, and our D84 estimates in the wetted channel are uncertain. Our low α values may reflect the roughness and rugosity captured in our detailed DEM, or the inherent limits in relating hydraulic roughness to simplistic grain size statistics (Adams, 2020). Tests with variations of the horizontal viscosity coefficient and our optical-empirical bathymetry relation confirmed no major improvements were found in those parameters.

Inundation frequency results (Figure 6a) are shown for a selected reach with an active and a wandering channel. There are 2-3 braids active at flows up to approximately 120 m^3s^{-1} over which side channels begin to flow. Under naturalized conditions, this flow would be exceeded for 73 days/yr, but is now exceeded for 43 days (upper abstraction) or 32 days (both abstractions). The mid-channel bars become fully inundated at flows above ~200 m^3s^{-1} (7-10 days/year). Near-complete inundation at ~1000 m^3s^{-1} occurs on average for ~8 hours/year.

The modelled inundation is compared with the wetted extent on the survey day in Figure 6b and Table 1. $Fit_{Congruent}$ results of between 0.85 and 0.93 compare well with previous studies (Javernick et al., 2018; Williams et al., 2013), and appear higher in the meandering reaches above km 46 which have a simpler planform. $FitW_E$ could not be fully calibrated to 1.0 due to the abundant hyporheic flow paths, side springs, and disconnected wet areas classified on the braidplain. The match between our observed and modelled water mask appears reasonable. The model overpredicts some intra-bar flow paths and misses some backwaters and/or spring-fed side channels. Additional maps supporting this comparison are presented in the supplementary material, including a qualitative comparison between satellite imagery and models during a higher flow event.

Table 1.

Model validation results.

Reach	Inundation		Depth			Velocity		
[km]	$Fit_{Congruent}$	$FitW_E$	RMS	Skill	Bias	RMS	Skill	Bias
56–46	0.931	0.973		-	-		-	-
46–38	0.914	0.956		-	-		-	-
38–31	0.896	0.969	0.223	0.790	-0.138	0.432	0.749	0.038
31–24	0.916	0.974	0.180	0.875	-0.109	0.447	0.794	0.060
24–18	0.852	0.911	0.195	0.801	-0.082	0.482	0.707	-0.010
18–12	0.899	0.951	0.193	0.871	-0.120	0.398	0.854	0.062
12–2	0.876	0.936		-	-		-	-

The aDcp survey provides an independent estimate of depth and velocity (Figure 6d,e) at the track taken by the raft (Figure 6a). Data acquisition was not complete, with the instrument lifted to safety over particularly turbulent sections and a navigator's bias towards travelling the larger braid. The model's skill in reproducing aDcp depth exceeds 0.79, with velocity skill between 0.70 and 0.85, with a 0.10 m depth bias and a near-zero velocity bias. The velocity is constrained in some channels by the grid resolution. We also do not explore velocities outside of the thalweg, so our comparison may be biased towards the areas of highest velocity.

Comparisons of celerity during events of $Qw = 65$ and 430 m^3s^{-1} showed the modelled flood wave travelling the 36 km distance in 5.0 to 3.5 hours. Travel time during an observed 1000 m^3s^{-1} event was 3.5 hours, while a 60 m^3s^{-1} observed event had a 7.1 hour lag. The modelled celerity is thus somewhat higher than observed. While models with higher α had longer transit times, processes such as infiltration also are unsimulated. A full treatment of the model calibration and validation is omitted for brevity. While all three metrics are reasonable, our final parameter choices were based on minimizing velocity bias as ours is a sediment transport study and small changes in inundation and event timing are immaterial.

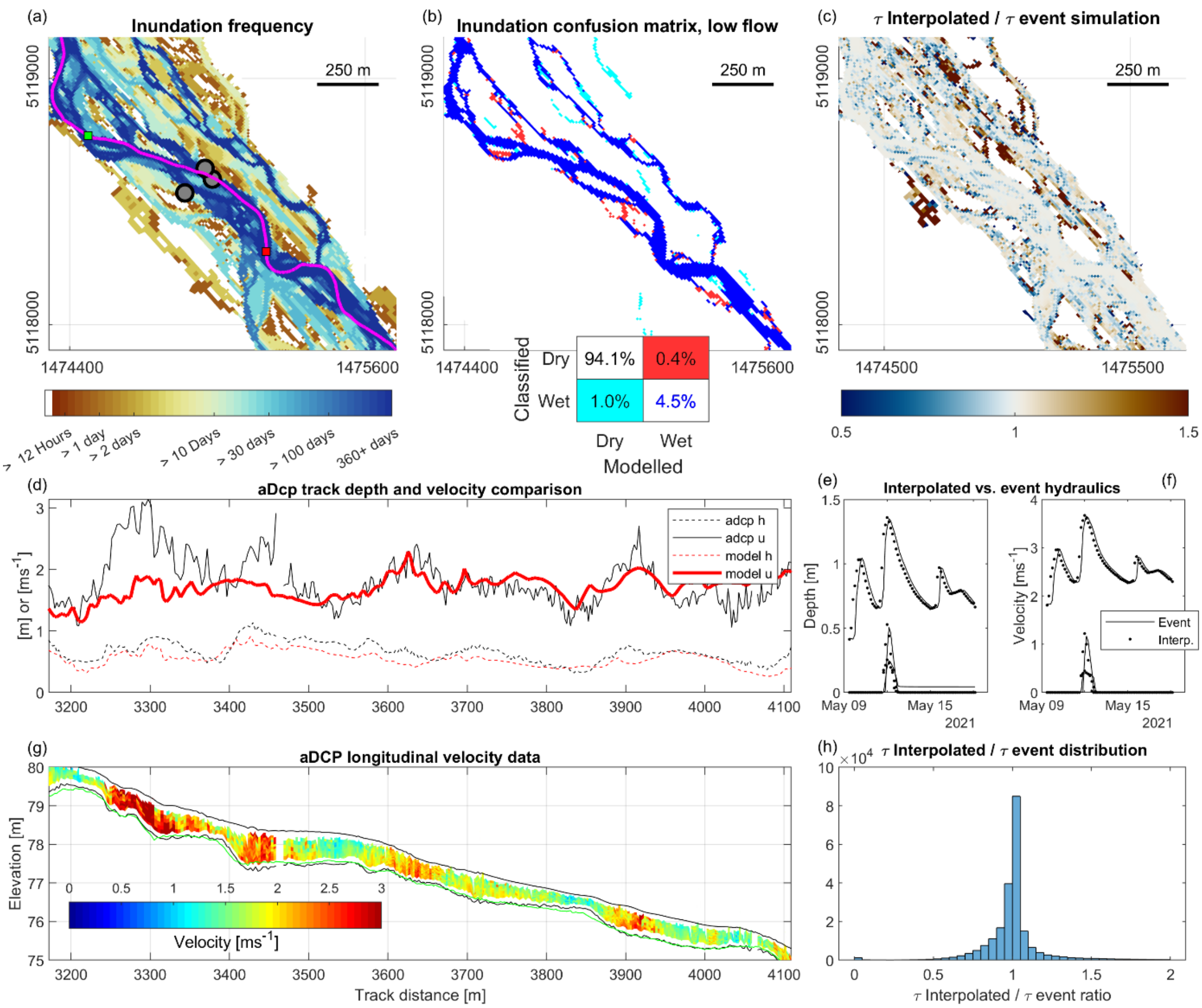

Figure 6 - Model Results (a) Inundation frequency, in days per year under a flow regime with one abstraction. (b) Confusion matrix and map of the same (c) Velocity and depth comparison along the aDcp path (d) Pseudocolor plot of aDcp velocities and depths. Section starts at green square on (a). The worst mismatch in this example is near 3300 m on the longitudinal section, corresponding to a chute 12 m wide, converging with spillage over a submerged longitudinal bar which forces the thalweg against a cut bank

The accumulation of shear stress in the model over a series of flow events is compared between the flow library interpolation and a time-stepping event simulation (Figure 6c). Depth and velocity comparisons at three select points (Figure 6e,f) show an expected temporal lag, but no major differences in value. The distribution of the τ-interpolated / τ-event ratio (Figure 6h) shows good agreement, with 91% of the domain's grid cells having a ratio between 0.5 and 1.5. The interpolation tends high in side channels, where lag and attenuation may reduce the flow of real events. The event simulations tend higher at some main channel edges, as continuity ensures that any reduced flow in side channels must then be compensated in the wetted channels.

https://doi.org/10.5194/egusphere-2026-2149
Preprint. Discussion started: 4 May 2026

4.1.2. Model Demonstration

Sediment capacity behaviour at a station

We demonstrate how the model behaves over a range of flows at three archetypical points in Figure 7. This figure shows how local GSDs and modelled hydraulics predicted sediment transport and local annual transport capacity. These locations (see Figure 3) represent the spatial variability of at-a-point sediment capacity using our base case model, which has complete spatial GSD estimates over 90% of the braidplain, longitudinal GSD estimates and 10% sand cover in the submerged regions and uses the GW14 sand exposure formulation (Run 257 in Table 2). The sediment capacity at each point is compared with the estimate of sand supply from upstream (Figure 2d).

Point 1 in the thalweg (a,d,g,j) has an estimated GSD and sand fraction. Depth, velocity and shear stress increase quickly with flow until ~250 m^3s^{-1}, above which width increases more than velocity. Even with an assumed bed Fs of 5%, suspended transport potential is an order of magnitude above supply throughout the hydrograph. Gravel transport increases until equal mobility is reached at 150 m^3s^{-1}. Point 2 (Figure 7b,e,h,k) is on the side of a main channel, 10 m from the low-flow bank and 1.7 m higher than Point 1. This location is wetted at flows above 250 m^3s^{-1}. Bedload sand transport, even with Fs=38%, is not sufficient to transport the incoming load, and suspended transport is sufficient only after 450 m^3s^{-1}. The deficit in potential sand transport between wetting and 450 m^3s^{-1} occurs for ~6 days/yr, and competent transport occurs for a further 2.4 days/yr. Equal mobility of the cobble fraction is not achieved within the flows modelled. Point 3 2 (Figure 7c,f,i,l), in a dry braided channel 25 m from the opposite bank and 1.1 m above the first point is also wetted above 250 m^3s^{-1}, but after an initial bedload burst is somewhat backwatered until a flow of 500 m^3s^{-1}. The combination of bedload and suspended sand transport never catches up to supply, even assuming the observed high bed Fs.

https://doi.org/10.5194/egusphere-2026-2149
Preprint. Discussion started: 4 May 2026

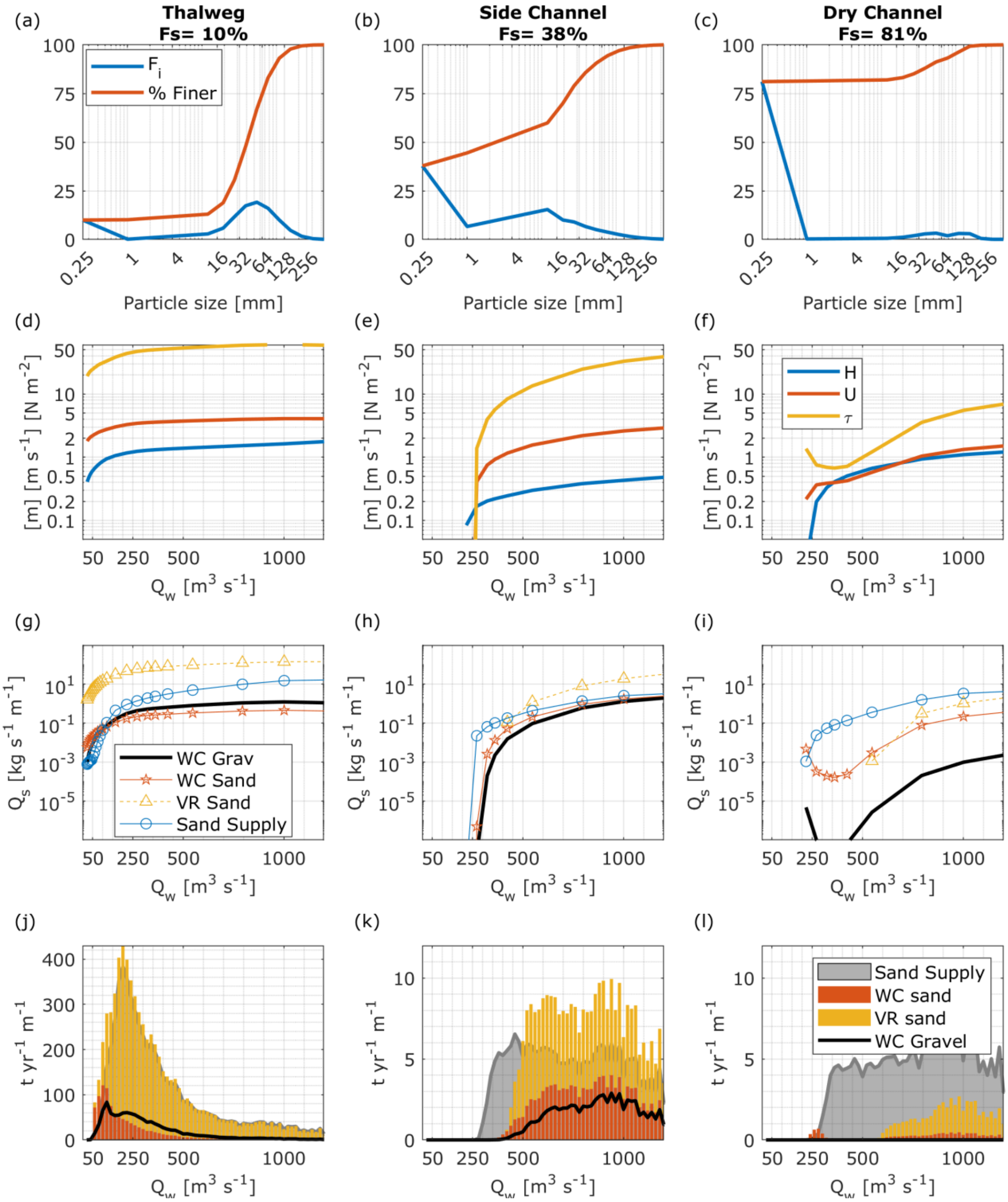

Figure 7 – Sediment transport predictions at thalweg, side of channel and dry braided channel example (1-3 on Figure 3). (a-c) Estimated GSD, with sand fraction Fs. (d-f) Modelled hydraulics vs. flow at each point. (g-i) Predicted sand and gravel fluxes and sand supply vs flow. (j-l) Sediment capacity vs flow, with van Rijn (VR) suspended load limited by Fs, hiding and supply and WC bedload sand and gravel limited by GSD, hiding and Fs.

Sediment transport capacity at a reach

Figure 8 shows the reach-integrated rates of gravel and sand capacity in tons/year (Equation 22) for two reaches using our base case model (Run 257) and the 40-year period of record hydrology with the upper flow abstraction in place. To summarize the long-term capacity relative to supply, we plot both supply and capacity as a width-normalized histogram with 20 m^3s^{-1} bins. This plot highlights which parts of the flow history may have a mismatch between supply and capacity.

The estimates of WC bedload sand transport *Qb* are well short of the supplied sand load at flows over ~100 m^3s^{-1}, with suspended sand capacity required to meet the supplied load. Since we limit suspended capacity with the inflow concentration assumption (Eqn. 8), the only way for the capacity to exceed supply in this model is for *Qb* to be greater than *Qin* – *Qs*. In other words, we accept that a near-unlimited quantity of suspended sediment could be carried in certain parts of the river – i.e. the main channels, but this excess capacity can quickly deplete the local bed and be locally supply limited, while at the same flow other locations can be capacity-limited.

The upper reach at KM 40 carries a peak bed sand load at a flow of 100 m^3s^{-1}, a broad peak in gravel load around 130 m^3s^{-1}, and a broad area of effective suspended sand transport peaking around 200 m^3s^{-1}. There is a total sand transport deficit from 120-600 m^3s^{-1} compared to the incoming load estimated at the gorge. The general pattern is similar at KM 10, despite the higher braiding index. There appears to be excess bedload sand capacity below 100 m^3s^{-1}, but this capacity is potentially wasted as the main braid bed will become armoured at these moderate flows. There remains a sand transport deficit relative to the upstream supply (which has been reduced slightly by the same abstraction) between 120-400 m^3s^{-1}.

Spatial information about areas of sand capacity competence or deficit at different flow levels can be interpreted from the maps (Figure 8a,c), which show potential deposition or erosion of sand in metres per year. These rates should not be interpreted as actual deposition as evolution of bed Fs with time would feed back into higher or lower transport rates. The mapped flow (273 m^3s^{-1} at the gauge, and 240 m^3s^{-1} after abstractions) represents the peak of the incoming sand load, and 11% of this flow was abstracted at the top of the reach. Many side braids and backwaters are in deficit, incapable of transporting the estimated concentration at this flow. Similar spatial patterns appear at other flows. Some side channels are more competent at lower flows as incoming concentration decreases and bedload sand transport continues; others become backwaters with their sedimentation potential dependent on connectivity. Section 4.2 demonstrates, with similar plots, how these results change after the mid-reach abstraction and with the natural flow regime.

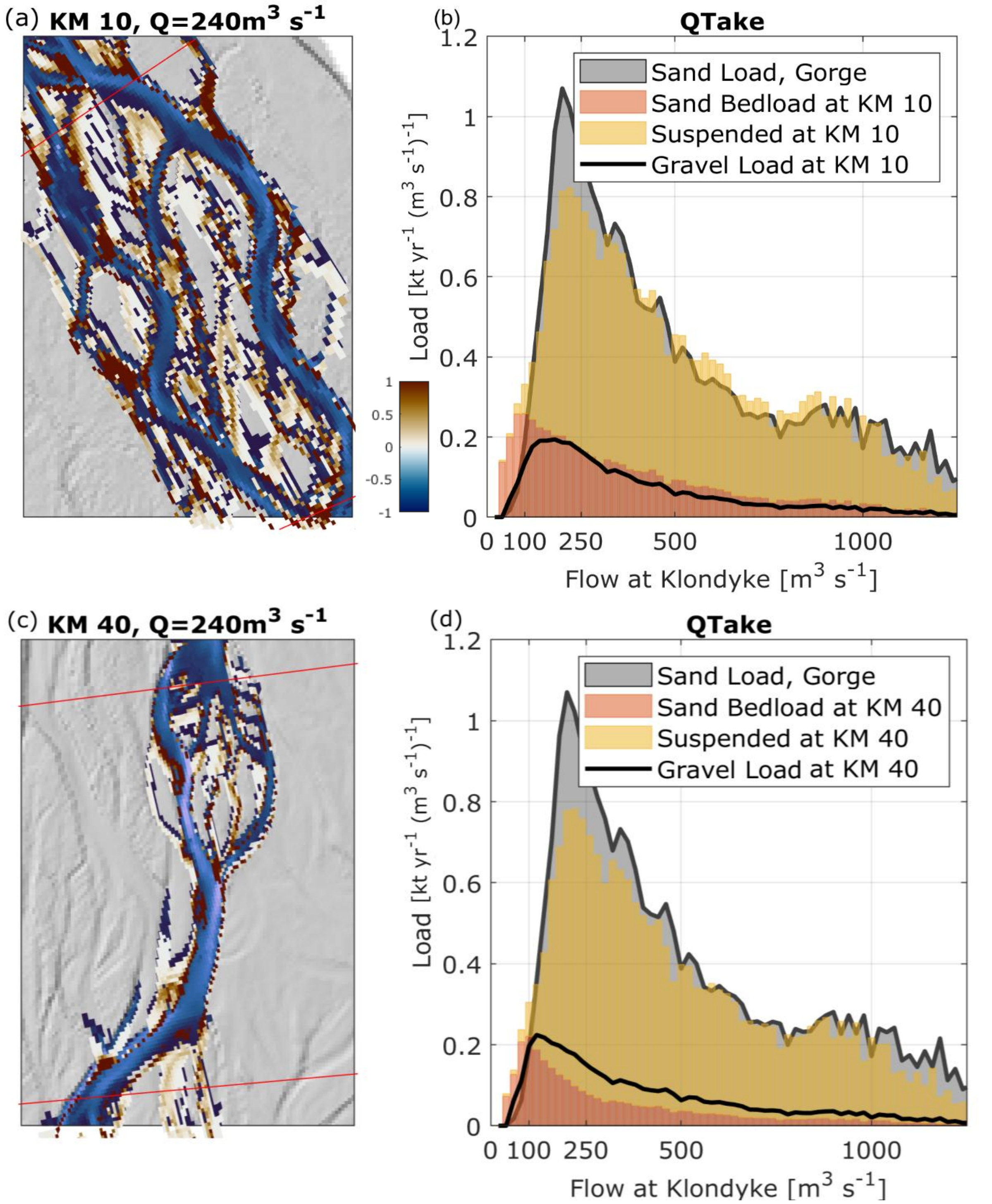

Figure 8 - Results of model scenario 257 at KMs 10 (a,b) and 40 (c,d). This model uses facies-derived D50 and Fs on the subaerial braidplain, longitudinal estimates of D50 and Fs=10% in the channel, and ξmax of 20 with the GW14 sand exposure correction. (a,c) Potential sand deposition, in m/yr. Where no deposition is predicted, flow depth in blue shades. (b,d) Reach-integrated sediment capacity vs flow, with suspended load limited by supply from upstream (gray, see Figure 2). The y-axis units are annual gravel flux per unit discharge interval, so the area under the curve over a discharge range gives the annual gravel load from that part of the hydrograph.

https://doi.org/10.5194/egusphere-2026-2149
Preprint. Discussion started: 4 May 2026

4.1.3. Sensitivity Analysis

Model parameterization experiments

The modelling framework presented above enables sediment transport capacity to be parameterized flexibly depending on the availability of supporting data. For example, in the absence of detailed spatial information, the bed composition can be represented using globally uniform values for the gravel framework grain size (D50) and the sand fraction (Fs) and alternative transport formulations with fixed hiding parameters. However, where spatially distributed substrate data are available (e.g., from a classified facies model), these crude assumptions can be replaced with facies-specific GSDs sand fractions.

Sensitivity tests were conducted in three major categories: (i) gravel, (ii) sand, and (iii) hiding/exposure, with 432 experimental combinations detailed in Table 2. We test the utility of spatial substrate data by simulating transport with combinations of D50 and bed sand fraction *Fs*, starting from constant values and D50 and *Fs*, then testing spatially D50 based on our facies map. The GSD of the submerged bed is tested with the longitudinal piecewise fit (Figure 4). The uncertainty regarding the submerged sand fraction is addressed by testing six different constant sand fractions in the low-flow channels. The interactions between gravel and sand are tested with different hiding and exposure formulations.

If we assume our knowledge of the subaerial bed is sufficient, we are still left with an unknown GSD in regions that were submerged during the survey. In the absence of better information, we test the longitudinal D50 estimate with constant sand fractions in these channels. The sensitivity tests for the submerged Fs assumption involved setting these areas to a constant 5%, 10% or 20% sand.

Table 2.

Sediment capacity model experiments

1st Digit	Gravel D50	2nd Digit	Sand %	3rd Digit	Hiding/Exposure
1	Constant	1	Constant Fs= 5%	1	Max Hiding=1
2	Facies	2	Constant Fs=10%	2	Max Hiding=10
3	Constant * 0.5	3	Constant Fs=20%	3	Max Hiding=20
4	Constant * 2.0	4	Facies Fs, Wetted Fs=5%	4	Max Hiding=40
5	Facies * 0.5	5	Facies Fs, Wetted Fs=10%	5	G&W, Max Hiding=1
6	Facies * 2.0	6	Facies Fs, Wetted Fs= 20%	6	G&W, Max Hiding=10
		7	Facies Fs, Wetted Fs= Fs 1%	7	G&W, Max Hiding=20
		8	Facies Fs, Wetted Fs= Fs 50%	8	G&W, Max Hiding=40
		9	Facies Fs, Wetted Fs= Fs 15%		

Note: Sensitivity tests were completed for the 432 combinations of the above options. The table is read such that "Run246" has "2:" spatially varying D50 (Figure 4c), "4:" the facies-based sand fraction applied to each cell that was dry during the survey, 5% sand fraction under water classes, and "6:" maximum hiding ξ=10 and the exposure correction of Grams and Wilcock (2014).

Sensitivity results: longitudinal gravel capacity

The sensitivity results are presented in terms of longitudinal patterns in estimated gravel capacity, with capacity vs. flow curves compared in the discussion. The longitudinal patterns show whether bedload is steadily transported throughout the reach or indicate where deficits (negative slope) or surpluses (positive slope) may develop. The plots in Figure 9 compare the modelled capacity of gravel bedload (>2mm) according to the WC equations, summarized in each reach, for selected sensitivity tests. If we apply a constant D50 of 50 mm, the gravel capacity reduces by an order of magnitude (250 to 25 kt/yr) over the reach (Figure 9a). A D50 sensitivity test results in factor of 6 mean reduction in transport when D50 is doubled, and 3x increase when the assumed D50 is halved, consistent with nonlinear responses to grain size in the WC equations. Varying D50 and GSD spatially (Figure 8b) produces more similar transport rates longitudinally, as we are more correctly describing the size of the bed material in each reach. Doubling [halving] the D50 we use in the WC equation, but this time retaining the spatially estimated GSD, produces a similar magnitude change to the constant test. This result is somewhat unphysical as the altered D50 is inconsistent with the underlying GSD.

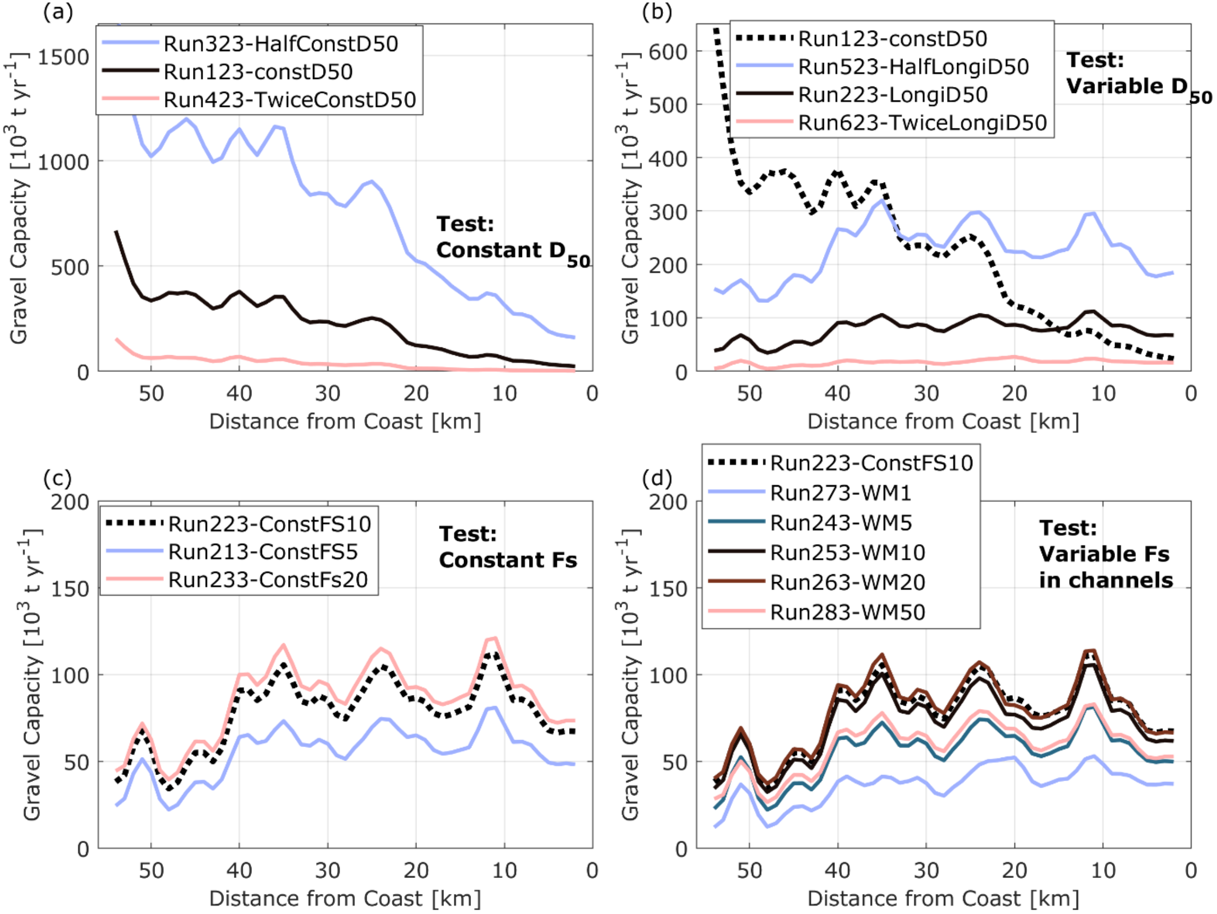

Figure 9 – Longitudinal Gravel Capacity Sensitivity (a) to a constant D50, +/- 100% (b) to a facies-based variable D50, (c) to a constant Fs with facies-based D50 and (d) to facies-based Fs with varying Fs under the low flow water mask. Note: the y-axis scale decreases from (a) to (c) with each panel retaining one line from the prior plot.

The effect of sand, applied uniformly, is tested in Figure 9c, with the 5-20 range in *Fs* representing the greatest area of change in the WC hiding formulation. The *Fs*=10% case has 40% more gravel transport than Fs=5%, while an increase from *Fs*=10 to 20% adds an additional 10% of gravel transport. Finally, we use our facies-based estimate of sand everywhere except the low-flow channel, and widely vary Fs where we have no observations (Figure 9d). Sand fractions of 1% and 5% produce lower gravel transport, while a *Fs* of 50% is much the same as 5% because we have added so much sand that we reduce the quantity of gravel available to move.

Sensitivity results: longitudinal sand capacity

The longitudinal patterns in estimated sand transport potential predict whether the incoming sediment load at the gorge exceeds, falls below, or matches the carrying capacity of each reach, and indicate trends of deficit or surplus. Figure 10 portrays both bedload and total transport of a 250 μm sand, for a range of sensitivity tests. The modulation of bedload sand transport with globally-constant D50 and GSD (Fig. 10a) occurs primarily through hiding and exposure in both the WC model (Eqns. 4-6), with a threefold increase in bedload sand when D50 is halved and a 2x decrease when D50 is doubled. The bed D50 has no effect on the suspended transport in this test because the sand fraction is unchanged and the Di/D50 ratio is saturated by both the ξ_{max} of 20 (Eqn. 11) and the SSC limit (Eqn. 8). There is a factor of 2 longitudinal decrease in total sand capacity with constant D50, driven by the widening hydraulic geometry. Allowing D50 and bed GSD to vary longitudinally but holding *Fs* constant (Fig 10b) reduces the longitudinal decrease to ~40% as downstream fining of gravel weakens hiding effects. Doubling/halving the gravel D50 has similar effects on bedload transport to the constant case and minimal effects on suspended capacity.

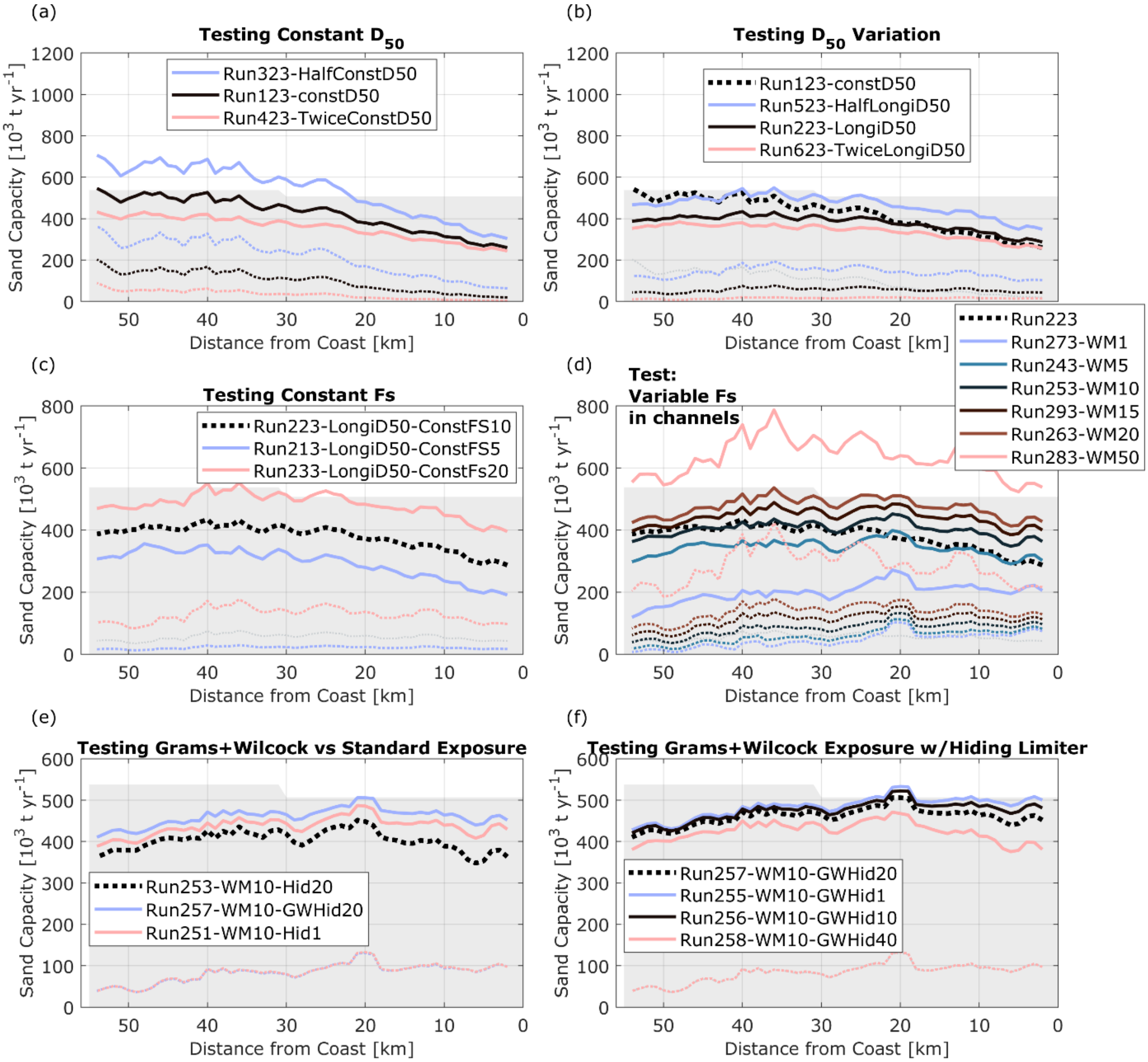

Figure 10 – Longitudinal Sand Capacity Sensitivity (a) to a constant D50, +/- 100% (b) to a facies-based variable D50, (c) to a constant Fs with facies-based D50, (d) to facies-based Fs with varying Fs under the low flow water mask, (e) to the exposure correction of Grams and Wilcock (2014), and (f) to the value of the grain hiding limiter. Note: the y-axis scale decreases in each row with every panel retaining one line, dashed, from the prior plot. Thicker lines are total transport; thinner dashed lines are only the bedload component, with suspended transport making up the difference. The grey shaded area in each plot represents the incoming sand load at the gorge and its mid-reach abstraction.

4.2. Model Application: Rangitata River altered hydrology

We now use our baseline model to compare the effects of altered hydrology on sediment transport. The examples in Section 4.1.2 included a single flow abstraction at the top of the study reach; Figure 11 compares this result with no abstractions or two-abstraction flow timeseries. A naturalized flow series on identical bed conditions could transport 43% more gravel on average, while introducing the flood-harvesting take at KM 31 reduces this model's gravel capacity by approximately 8% (Figure 11a). The effects on the sand capacity (Figure 11b) are similar, with naturalized flows capable of carrying 23% more sand and the second abstraction also reducing sand transport by 8%. When simulating the RS flood harvesting abstraction, the abstracted sand load is not reintroduced to the river, so the load curve (grey) decreases at KM 31, but the capacity curve reduces further.

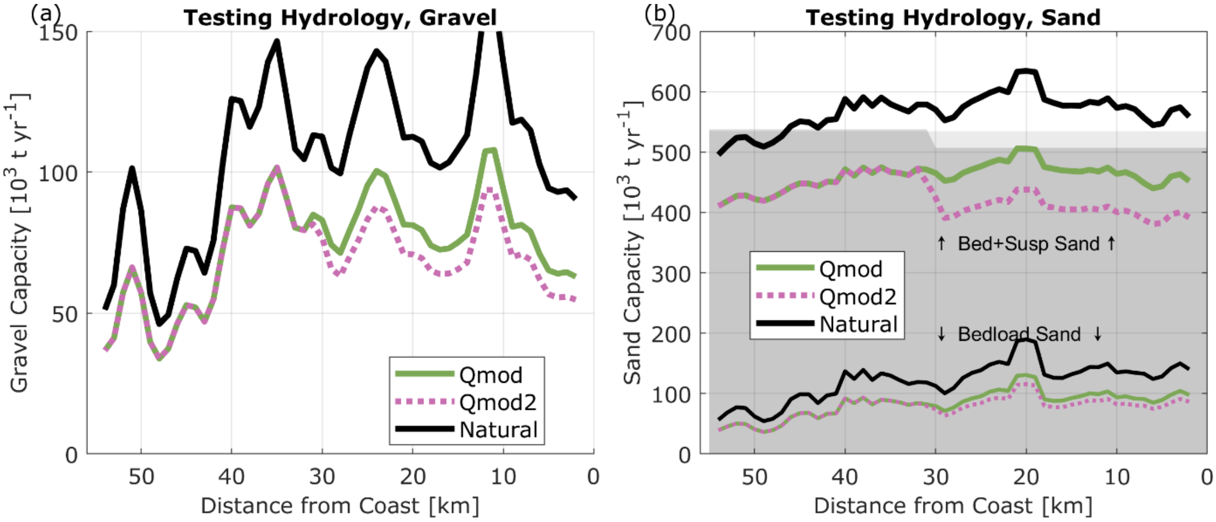

Figure 11 – Sensitivity of longitudinal transport of (a) gravel and (b) sand to different hydrologic regimes. Natural = Naturalized flow regime with no abstractions. Qmod: One abstraction (RDR) at the top of the reach. Qmod2: Both abstractions, adding the RS flood-harvesting at km 31. For (b), bedload sand is the lower set of lines, and the total transport is the upper set. The incoming sand load is represented by the grey background.

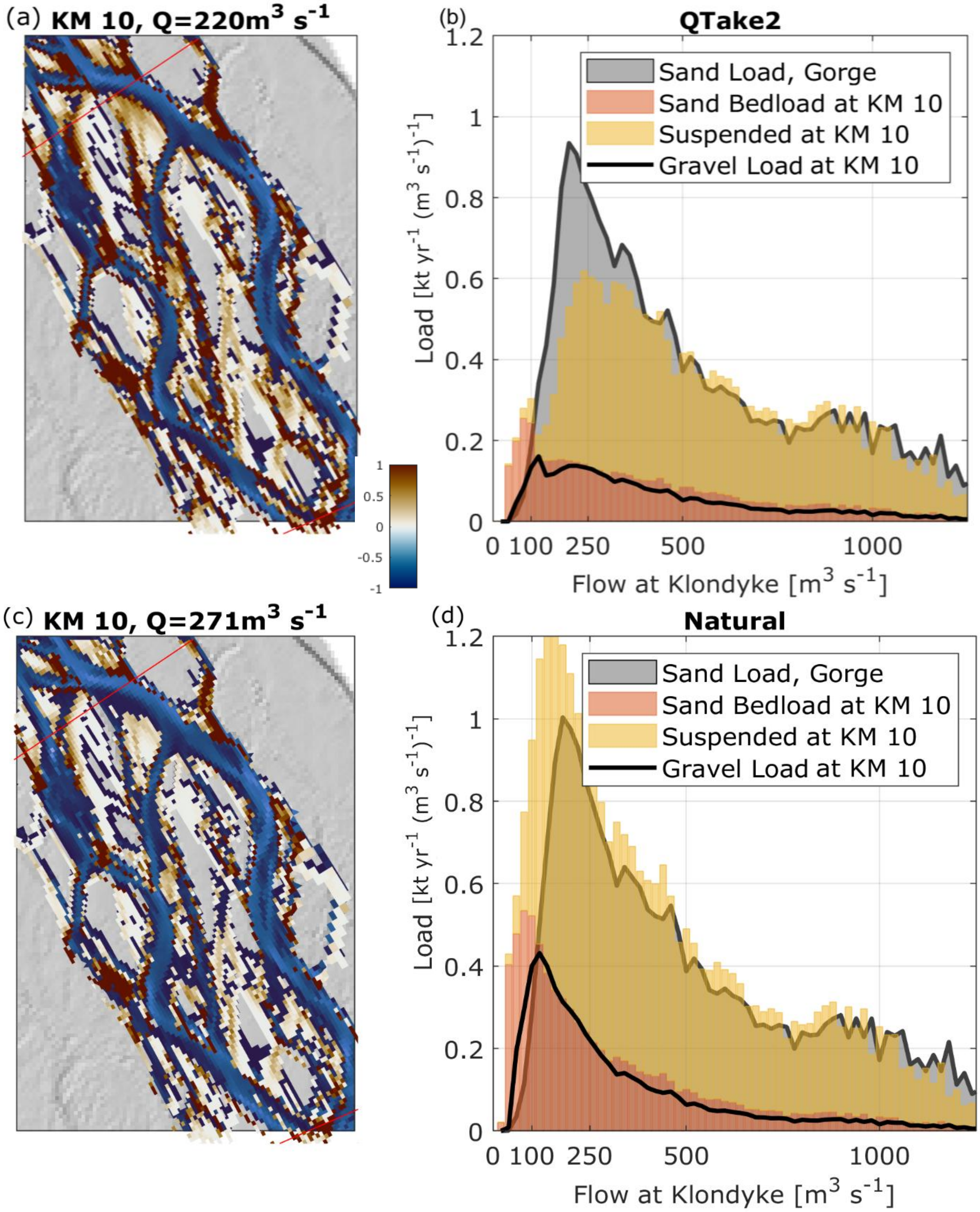

Figure 12 - Potential sediment transport under Naturalized and flood-harvesting flows. As per Figure 8c,d. which had one abstraction, but with Natural = Naturalized flow regime and Qmod2= Both RDR and RS abstractions. Where no deposition predicted, flow depth in blue shades

In Figure 12, we revisit the Q-capacity plots and the sand transport deficit maps of Figure 8c,d (flow series with a single abstraction) to compare capacity for fine sediment transport with (i) naturalized flows or (ii) both abstractions to the same reach. The naturalized flow regime appears capable of meeting the supplied sediment load at almost all flows, especially those in the intermediate range that was in deficit with the first abstraction (Fig 12b). When the second abstraction is applied, there is a further loss of capacity above 100 m^3s^{-1}, expanding the flow range over which there is a deficit relative to supply (Fig 12d). The maps of sediment deficit under natural flows still have areas of potential sand deposition (Fig 12a), but many side braids have a continuous transport pathway. After the RS abstraction (Fig 12c), only the two main braids appear to have continuous sand transport, with a reduction in area and capacity leading to potential deposition in side channels.

Retaining the facies-based GSDs and D50 and applying a constant sand fraction (Fig. 10c) produces 30% sensitivity in total transport when halving or doubling bed Fs, driven in equal absolute proportions by bedload and suspended transport. A slight longitudinal decrease in sand transport is apparent past KM 40, where the river changes from meandering to braided form. Figure 10d applies the spatially-varying Fs on the subaerial bed, and tests the sensitivity of Fs assumptions in the low-flow channel. The longitudinal transport trend in the lower 40km is largely flattened with these additional data. The bedload WC equations cannot carry the given load, even if assuming a 50% Fs. Suspended transport reaches an asymptote after Fs~=15 as our SSC limits are reached, while bedload sand transport responds linearly to Fs. The total transport is particularly sensitive to the choice of channel sand fraction, which is expected to evolve during flow events.

Exposure and hiding parameters are tested with a constant wetted channel Fs of 10%. Figure 10e demonstrates increased suspended sand transport with the GW14 bed sand coverage function (Eqn. 16). Inclusion of this exposure correction increases total transport by 14% as the area of competent flow expands. This is a larger change than the 8% increase in Run251 which does not have the GW14 exposure correction but eliminates the hiding factor. Finally, we examine the hiding limiter in Figure 10f, retaining the GW14 exposure equation. Reducing ξ_{max} to 10 or 1 only increases transport by 5 or 3% respectively; a doubling of ξ_{max} to 40 drops total transport by 8%.

5. Discussion

5.1. Importance of spatial bed data to gravel transport

This study provides insights on the contribution of spatial bed data to sediment transport over a long reach. Laboratory studies that model bedload do not consider the strongly bimodal facies we find in the field (Javernick et al., 2018; Redolfi et al., 2018), while field-scale work in similar rivers uses vastly simpler GSD and morphology assumptions (Nicholas, 2000) or much smaller reaches (Vericat et al., 2008). The modelling study of Singh *et al.* (2017) found that high sediment heterogeneity helped produce realistic bar morphology and a diversity of channel GSDs, whereas we avoided evolving the bed morphology in favour of novel classification-based GSDs and a regional approach to bedload and suspended sand transport.

Although we assume steady state conditions, our 56-km reach includes a full range of possible channel forms. We believe that testing longitudinal consistency in transport over our large and morphologically diverse study site is a useful test, despite the limitations of a single temporal snapshot and a static bed assumption. Our resolution of sediment patches was informed by the field experiments of Vericat *et al*. (2008), who used a portable flume to test sand patch depletion and found a threshold near 30 N/m² where sand loss increased. The three example locations in Figure 7g-i illustrate the necessity of spatial hydraulics; the thalweg location is always over 30 N/m², the thalweg-adjacent location exceeds the same shear stress at Q>900 m³s⁻¹ (occurring once/year), and is never exceeded in our example dry braided channel.

As concluded by Monsalve *et al*. (2016), improving gravel transport estimation accuracy requires detailed modelling and measurements. Our model uses spatially explicit hydraulics, such that we can predict bedload transport at the low and moderate flows which dominate the hydrograph. Many studies confirm that the spatial variability of bed elevation and flow hydraulics are key factors in a braided river's sediment load, which is dominated by intense transport in small portions of the wetted area (Javernick et al., 2018; Monsalve et al., 2020; Nicholas, 2000). Since gravel transport is dominated by areas of the river for which we lack data, we can draw few conclusions other than to replicate the increased gravel mobility when we assume a high bed sand fraction (Figure 9c,d).

Our choice of a static bed has obvious limitations. Lateral mobility is the key to moving the material at our dry braided channel example location; gravel here is not picked up 'vertically' but eroded during avulsion or lateral migration events. Time-stepping geomorphic models can co-evolve geometry and composition to an equilibrium that satisfies the equations, realistically or otherwise, and even the most detailed 2D simulations still have difficulty in reproducing a realistic lateral

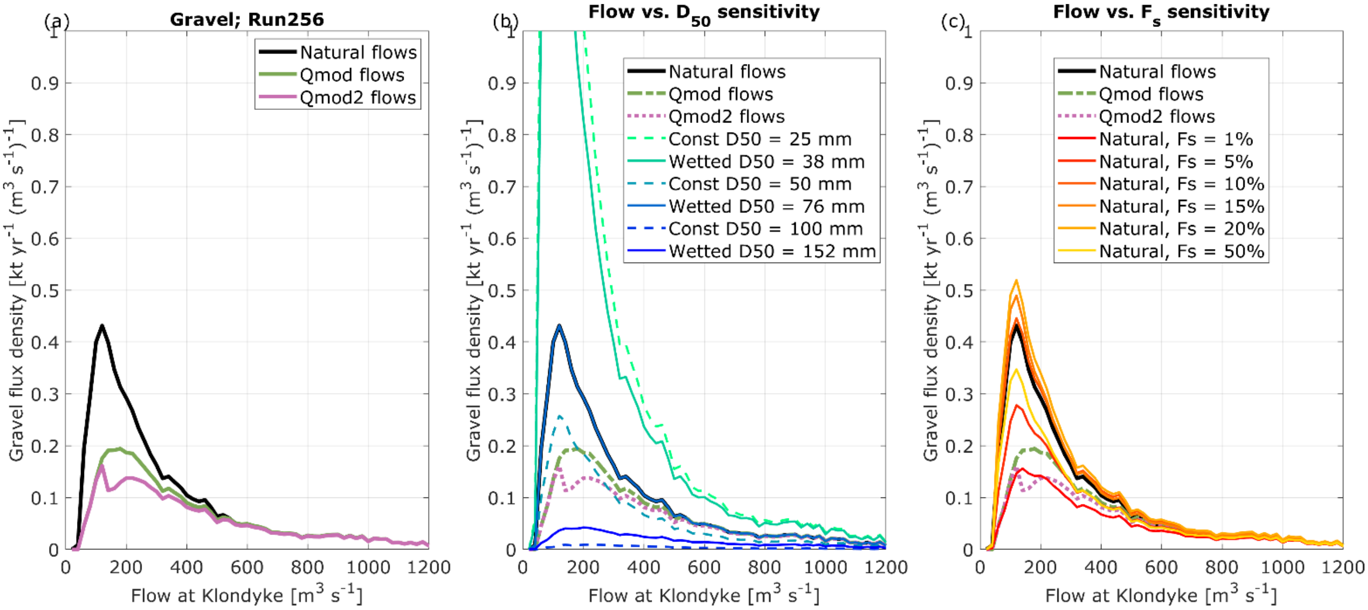

Figure 13 – Sensitivity of potential gravel transport at KM 10 to (a) the three flow regimes, using the same case as Figs 8b and 12b); (b) changes in bed D50, where Const = uniform D50 across domain and Wetted = facies-based D50 on the subaerial braidplain and constant values in the wetted channel; and (c) changes in bed Fs, with facies-based gravel D50. In panels (b) and (c), the flow scenarios for the baseline run (256) are repeated for comparison. The y-axis units are annual gravel flux per unit discharge interval, so the area under the curve over a discharge range gives the annual gravel load from that part of the hydrograph.

migration rate (Stecca et al., 2017). Static bed estimates by Nicholas (2000) use a gamma distribution to consider bedload transport of a uniform GSD in a large river, while Monsalve *et al.* (2020) partially addresses spatial complexity with a statistical distribution of shear stress and a single subsurface GSD. Our 2D-model driven approach is similar in that we are using local hydraulics to calculate a range of shear stress and transport rates before summarizing with a flow-weighted integral. Our method differs in that we also attempt to resolve local-scale GSDs with a ~10 m² aggregation of 1 m² surficial facies predictions. Our numerical experiments test the range from uniform, to longitudinally varying, to near-complete spatial mapping of GSDs and each tranche of additional data shrinks the uncertainty of our transport estimate.

The spatial patterns of gravel transport confirm prior field interpretations of the lower Rangitata River. Sensitivity tests of D50 imply that the river can easily transport the ~20 mm gravels coming from the upper catchment, as expected from the slope change from .002 to .006. We agree with Carson (1984) that the large clasts introduced as the river is constricted by glacial terraces favour stability of the meandering profile above KM 46. The valley slope lowers from 0.006 to 0.004 over the 56-km reach (Figure 1), the braidplain widens by a factor of 3 (Figure 4b), and the braiding index increases. With an unrealistically constant D50 and uniform Fs=10%, we see the expected pattern of decreasing bedload transport with downstream distance driven by the widening and slowing hydraulics. When we include the observed downstream fining pattern with spatial GSDs, there is greater longitudinal consistency of reach-averaged sediment transport and the meandering-braided transition at KM 46 appears as a step change in apparent capacity (Figure 9b). In flow vs. capacity plots (Figure 13b), moderate changes in D50 on the braidplain produce changes in transport of the same order of magnitude as the flow scenarios, while the extreme (doubled/halved) D50 scenarios far exceed the hydrologic variability. D50 changes mainly shift transport up or down, while alterations to the flow regime change the discharge band where transport capacity peaks by 80-100 m³/s.

Bedload gravel transport is sensitive to the sand fraction, which we have tested with constant values covering the most sensitive range of the WC equations (Figs. 9c, 13b). Field observations in the main channel remain difficult, but pebble counts during low-flow between KM 8-12 (ESNZ, unpublished, see supplemental data) indicated that main and side braids rarely had more than 10% sand. Adding our spatial estimates of bed Fs slightly decreases gravel transport (Figure 8d). Our predictions are within the 50-100 kt/year range estimated by Healey (1997). In flow vs. capacity plots (Figure 13c), the sensitivity of gravel transport to Fs produces changes in total transport, but only weakly affects the flow representing the peak capacity compared with the larger shifts due to hydrologic regime.

Taken together, the longitudinal and flow-space comparisons show that bedload gravel transport depends strongly on how the bed is represented, even though the main aim of the modelling is to better constrain the transport of the fine fraction. Spatial bed data is needed to produce consistent longitudinal gravel estimates, with the critical caveat that sustained higher transport rates predicted on our static bed would quickly result in bed armouring. The gravel aspects of this work could be better tested with repeat surveys or application in a system with better sediment load validation data.

5.2. Consideration of fine sediment

Sand-sized sediments travel both as bedload and suspended load in this river, at different locations and times. As seen in Section 4.1.3, bedload-only models, even with high estimates of submerged *Fs*, are unable to carry the incoming sand load. When we attempt to correct for this by adding suspended transport, we find that the thalweg could carry the entirety of the suspended load if not limited by bed composition, hiding, and/or upstream concentration. We also find that at the same flows, there are many areas which would not have capacity at the present bed composition to carry the incoming SSC and thus likely deposit fines. A bed facies map, and sensitivity-tested estimates of submerged sand content, helps to better constrain the transport capacity of a reach subjected to different hydraulic forcing. The "intense … modelling and detailed field measurements" suggested by Monsalve *et al*. (2016) for gravel estimation are also critical for reducing the uncertainty in sand transport.

Experiments with constant D50 and *Fs* (Figure 10a) show a gradual decrease in sand capacity downstream, dominated by changes in bedload transport. The trend moderates when longitudinal D50 information is provided (Figure 10b), but with constant Fs=10% there is still a loss of capacity downstream and the changes in gravel D50 just alter the rate through the WC hiding calculation. Adding the spatial bed Fs estimates (Figure 10d) was required to achieve a consistent longitudinal sand capacity, which is our metric of realism in this steady-state model.

The choice of hiding and exposure parameter has a large influence on the transport of fine sediment and is poorly constrained for a fine sand – cobble mixture. The flume work of Dudill *et al.* (2017) , while not reaching our sand/cobble size ratio, illustrates the breakdown of simple hiding relationships for high fine sediment feed rates in a mobile bed, and the cobble-sand experiments of Grams and Wilcock (2007, 2014) show that hiding relationships fail without consideration of the exposure of sand patches on an immobile cobble bed, and their formulation achieves 90% of the pure-sand suspended transport rate at a Fs of ~19%. Applying the Grams and Wilcock (2014) exposure calculation (Figure 10e) enhances the transport capacity of bimodal patches in our braidplain map, allowing a slight increase in the potential sand transport as the area of mixed facies expands (Figure 4b). The transport increase may be larger if we applied the exposure correction to the bedload transport as well, or considered the time evolution of Fs during events, both of which are beyond the scope of this study.

Reducing limits on the hiding ratio can favour sand transport, while increasing the hiding ratio cancels out the additional exposure effect of GW14 over mixed facies. We attempt to define the uncertainties of these relationships, although do not fully explore the implications due to the concentration limits we have imposed on suspended transport. We recognize that the hiding calculation of McCarron (2019) is prototyped for a coastal setting with a lower size ratio, but chose it because our bimodal sand-cobble mixtures have a somewhat meaningless and unstable median grain size. We retain the GW14 exposure and a moderate ξ_{max} of 20 for our preferred model which has a reasonable longitudinal trend and approaches, but cannot exceed the observed sand load. The interaction of hiding, exposure and enhanced transport of sand amidst cobble, either stationary or moving, remains an uncertain and difficult phenomenon to observe in the field.

Our range of sensitivity tests can turn this combination of sand transport equations into a ‘fluvial equation of state’ for a given flow; in short, we can ask what bed composition would be required to consistently move the given sand supply. In our data-rich models, the river’s ability to transport sand increases downstream because the bed fraction of sand also increases downstream.

5.3. Changes in hydrology

A Rangitata River with a naturalized flow regime would still have sand deposits, but given the present bed composition, the annual sand transport capacity would increase. Using our capacity model, the predicted increase in sand capacity with a naturalized hydrograph is ~100 kt/yr (+23%) above the historical single abstraction hydrograph, and ~140 kt/yr (+33%) above the present-day hydrograph containing both the relatively constant upper and mid-reach flood-harvesting abstractions.

The effect of altered hydrology, in flow vs. capacity space, is to increase the peak effective discharge for transporting sand from ~120 to 220 m³/s (Figure 14a). The salient result when comparing our fine sediment capacity scenarios and the incoming rating curve is this change in peak effective discharge, and the mismatch in the ‘intermediate’ discharge range which carry the bulk of the incoming load.

Comparing these modelled changes to the bed Fs sensitivity tests, the effects of altered hydrology on the bed are comparable to a 10-15% change in the bed sand fraction (Figs 9d, 14c). The sensitivity to doubling gravel D50, via hiding mechanisms, is

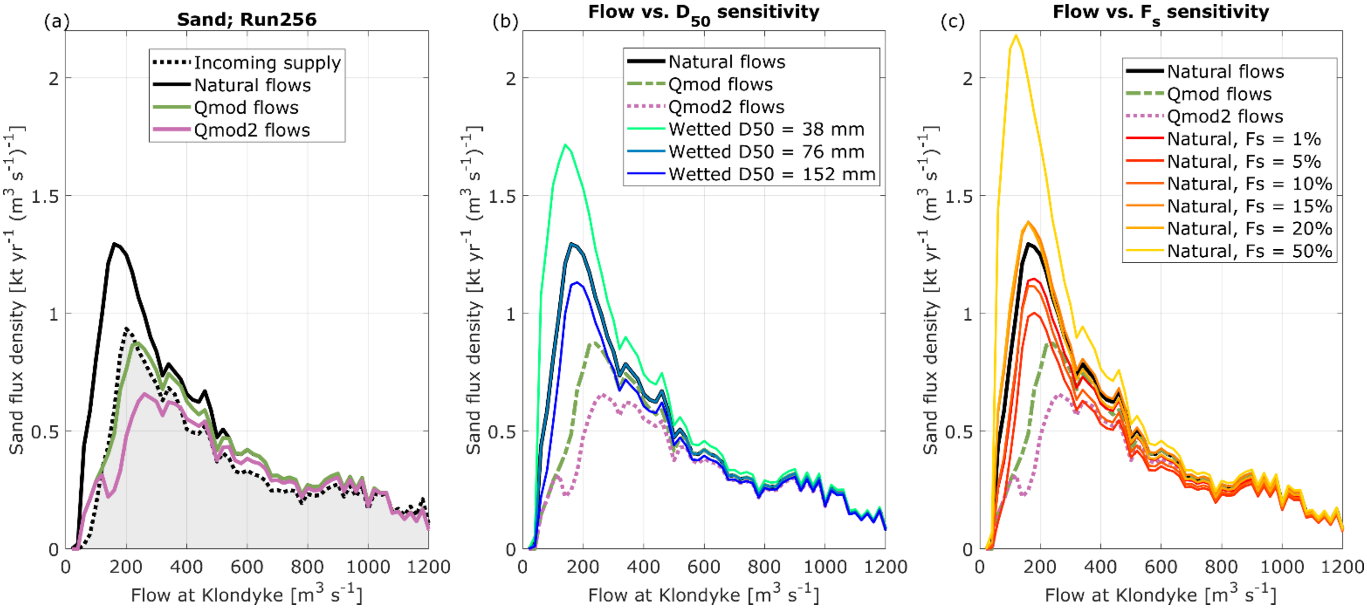

Figure 14 – Sensitivity of potential sand transport at KM 10 to (a) the three flow regimes, using the same case as Figs 8b and 12b) with incoming supply for comparison; (b) changes in bed D50 where the facies-based D50 on the subaerial braidplain remains unchanged but the constant values in the wetted channel are altered; and (c) changes in bed Fs, with facies-based gravel D50. In panels (b) and (c), the flow scenarios for the baseline run (256) are repeated for comparison.

similar to the capacity changes across our hydrologic scenarios. However, gravel framework D50 at a reach will not alter in response to flow changes as quickly as the bed sand fraction.

Considering the expanded Lane's balance of Dust and Wohl (2012), and a relatively constant valley slope, the river can respond to lower flows with a decrease in the width to depth ratio, or a fining of sediment size. Our model only considers substrate fining, and predicts that an increase in flow would reduce the amount of sand on the bed. We cover a wide variety of width-depth ratios in our domain as the braiding index varies by reach, with our spatial predictions of transport deficit consistently indicating that the areas with additional capacity would be in the smaller channels that are active at intermediate flows.

If our model remains consistent across a flow change, we can then estimate the additional area of sand facies required to balance the new flow regime. This method would require the time evolution and routing of sand in suspension, and therefore exceeds the goals set out in our two-dimensional modelling framework. However, the use of these spatial data in a one-dimensional modelling framework is the direction of future work.

To better understand this mismatch, we contrast the geomorphic setting of the lower and upper reaches. The Rangitata above the gorge is wider (1-2 km), lower in slope (0.002), relatively unconstrained and shows its own downstream gravel fining sequence which is interrupted at the gorge. Our study reach exhibits a resupply of coarse material likely sourced from glacial terraces. In the lower reach, the increased slope and coarser bed has formed a more armoured river whose transport capacity is dominated by its main braids, with less labile side channels at the same flows at these intermediate events. The lower river, under modified hydrology, cannot consistently transport the observed sand load because a portion of that load is distributed into channels that are incompetent with our observed bed composition, even with the most optimistic model assumptions. The upper river therefore likely has a different sediment storage and mobilisation response to flow than the lower river, leading to differences between the rating curve and downstream capacity.

5.4. Model methods limitations and perspectives

Changes in morphology and bed composition are a limitation of this capacity model. Gravel transport may be dominated by transient morphological events (Hicks et al., 2020), as many locally energetic pulses of sediment occur as channels migrate and bars and banks dissect and collapse. The utility of this work's spatial detail to gravel transport is reduced by the lack of morphological realism. On the other hand, sand can be deposited and scoured at moderate flows which do not mobilise the cobble framework. The true bed will continue to evolve in each event, with areas we identify as subject to deposition increasing in Fs and therefore future potential transport. Simulating the evolution of sand amongst immobile cobbles, such as the model of Haddadchi and Rose (2022), combined with sediment routing, could be used to allow our substrate map to evolve not in morphology, but in sand content. While transient morphological events surely affect the sand balance, our method's use of a near-complete bed GSD map produces a longitudinally-consistent and spatially-specific view of where deposition may occur. A reconstructed sediment transport history from the equilibrium hydraulics flow library provides a powerful tool for understanding different flow regimes despite the simplification of complex and interacting processes. Non-equilibrium transport can be seen at the study area boundary in the form of suspended sediment hysteresis, and concentration will continue to evolve down the river because of erosion, channel migration, or even abrasion. The main channels of our river during moderate flows have enormous capacity to transport suspended sand, and of the limiters we implement on equilibrium suspended concentration (hiding (Eqns. 9-12), bed *Fs*, and SSC_{Gorge} (Eqn., 8)), the upstream SSC has the greatest effect on the absolute value of transport. However, in steady state with no evolution or differences in concentration across the domain, increasing the SSC limiter does not change the relative locations of sand capacity deficits. Even with the most optimistic transport settings, there are always dead zones in this large, complex river, and assuming a growing incoming SSC simply results in a higher theoretical quantity of deposition.

Our major assumptions regarding fine sediment capacity are: (i) The rating curve at the gorge, itself downstream of a significant braided reach in the upper river, correctly represents the typical fine sediment concentration at each flow level, at every location; and (ii) The tremendous fine sediment carrying capacity of any area with cobble mobility means we can ignore the excess capacity of the main channels; only transport-limited areas reduce the reach capacity in our model. The patterns of diffluence and confluence in this braided river ensure that even as the main channels move tremendous amounts of sand, lateral dispersion still will introduce fine sediment to our areas of lower capacity. The same assumptions operate in the case of fine gravel from the upper catchment transiting the gorge and the upper ~10 km of our study reach; the steep, boulder-rich meandering section can carry a sufficient quantity of fine gravel when we artificially lower the bed D50 as may occur during a bedload pulse from the upper catchment (Figure 8a).

The preponderance of sand transport potential during low (<100 m^3s^{-1}) flows (Figs. 8d, 12b,d) represents 'wasted' stream power during supply limited conditions. While sand has been observed in the river's main braid during field surveys, it is well sheltered within coarse substrate. During low flow, clearer water downstream suggests continual filtering of the modest sand load (Jowett and Milhous, 2002). Channel morphology is essentially fixed during these flows. At higher flows, there are likely local depletions of SSC in wandering or widening channels, such that only the first few metres experience deposition; again with no evolution in concentration we can only predict susceptibility. Unfortunately, the difficulty of sediment load gauging in a braided reach during flood events precludes event-level validation, and the energetic Canterbury coastline destroys any geologic record of the river's sand delivery to the ocean. An expensive next step would be 3D time evolution of suspended sediment throughout our model. Event-scale simulations ran at a 3:1 simulation to wall clock ratio on 8 cores of a relatively powerful workstation (Intel i7-12700), which was viable for short events but not for long term simulations. Future efforts should focus on distilling and transferring as much spatial information as possible from this model and the river observations to a simpler framework that can consider change over time.

6. Conclusions

A two-dimensional modelling framework is used to ask whether the capacity of a large braided river to carry fine sediment changes with mid-range flow abstractions. This motivating question for the present study is spatially and temporally demanding, occurring over tens of kilometres and decades, with variability in time and space. Use of a fine sediment facies map and spatially explicit steady state calculations of bedload and suspended transport constrains the sand capacity, and produces a more consistent longitudinal trend in capacity. The reconstructed flow history allows us to efficiently test the tendency and magnitude of deficit, equilibrium, or surplus sand capacity in any location while varying parameters such as bed composition or hiding and exposure formulations.

The WC surficial sediment transport model cannot move the quantities of sand delivered by the catchment, requiring a model that considers sand as both bed and suspended load. The Van Rijn suspended transport model can achieve near-unlimited transport during higher flows in the main braids, and since we avoid the downstream evolution of concentration we chose to limit suspended transport by incoming concentration. This approach leads us to count areas of sand transport *deficit* but cannot realistically consider suspended sediment erosion; that is instead implied by the bedload transport rates. We cannot use this approach to consider the dynamics of sand in time without a time-stepping routing model, which would be prohibitive at this scale and resolution. Instead, we produce a detailed map of the areas susceptible to fine sediment deposition under different flow regimes. Future efforts include ways to simplify the rich spatial data herein to a form usable in a sediment routing model.

The model indicates that the bed is sensitive to the recent change in hydrologic regime, particularly in the side channels accessible during the common ‘moderate’ flows that occur for tens of days per year. Simulations comparing the river’s sand transport capacity under the present hydrologic regime with a naturalised hydrologic regime indicate that the impacts of the flow abstractions are comparable to a 10-15% change in the bed sand fraction, and that the effective discharge required to mobilise the incoming sand load has increased. Maps of potential sand deficit align well with observed depositional areas, and highlight the critical importance of intermediate flows and their alteration to the hydraulic and substrate characteristics of side braid channels and backwaters.

7. Data Availability

Bed sediment data, digital elevation model and substrate maps, along with selected model results are available from https://doi.org/10.6084/m9.figshare.32030595. Additional data that support this study are available from the corresponding author upon reasonable request.

8. Author Contributions

JR was responsible for method development, conceptualization, software development, analysis, visualization and writing. JH contributed conceptualization, supporting data, supervision and review. JB was responsible for funding acquisition, conceptualization, supervision and review. Thanks to Paul Bealing and School of Earth and Environment technical staff for supporting the surveys and acquisition.

9. Acknowledgements

The authors would like to thank Richard Measures, John Montgomery and Arman Haddadchi for field data and modelling suggestions. This work benefits from data collected by Environment Canterbury and the Rangitata Diversion Race.

10. Financial Support

JR was funded by Department of Conservation Postgraduate Scholarship, Grant/Award Number: 4799; JH was supported by Earth Sciences New Zealand, Future Freshwater Flagship Programme, Project FPFF2601; field work supported by Environment Canterbury, Ministry of Business, Innovation and Employment, New Zealand, Grant/Award Numbers: C09X1804, CAWX2101;

11. Competing Interests

The authors declare that they have no conflict of interest.

12. References

Abu-Aly, T. R., Pasternack, G. B., Wyrick, J. R., Barker, R., Massa, D., and Johnson, T.: Effects of LiDAR-derived, spatially distributed vegetation roughness on two-dimensional hydraulics in a gravel-cobble river at flows of 0.2 to 20 times bankfull, Geomorphology, 206, 468–482, https://doi.org/10.1016/j.geomorph.2013.10.017, 2014.

Adams, D. L.: Toward bed state morphodynamics in gravel-bed rivers, Prog. Phys. Geogr., 44, 700–726, https://doi.org/10.1177/0309133320900924, 2020.

Adams, J.: Contemporary uplift and erosion of the Southern Alps New Zealand, GSA Bull., 91, 110–113, https://doi.org/10.1130/0016-7606(1980)912.0.CO;2, 1980.

Altenau, E. H., Pavelsky, T. M., Bates, P. D., and Presented, A. T.: The effects of spatial resolution and dimensionality on modeling regional-scale hydraulics in a multichannel river, Water Resour. Res., 53, 1683–1701, https://doi.org/10.1002/2016WR019396, 2017.

Baker, D. B., Richards, R. P., Loftus, T. T., and Kramer, J. W.: A NEW FLASHINESS INDEX: CHARACTERISTICS AND APPLICATIONS TO MIDWESTERN RIVERS AND STREAMS 1, JAWRA J. Am. Water Resour. Assoc., 40, 503–522, https://doi.org/10.1111/j.1752-1688.2004.tb01046.x, 2004.

Bales, J. D. and Wagner, C. R.: Sources of uncertainty in flood inundation maps, J. Flood Risk Manag., 2, 139–147, https://doi.org/10.1111/j.1753-318X.2009.01029.x, 2009.

Brasington, J., Vericat, D., and Rychkov, I.: Modeling river bed morphology, roughness, and surface sedimentology using high resolution terrestrial laser scanning, Water Resour. Res., 48, https://doi.org/10.1029/2012WR012223, 2012.

Bright, C. E., Mager, S., and Horton, S.: Response of nephelometric turbidity to hydrodynamic particle size of fine suspended sediment, Int. J. Sediment Res., 35, 444–454, https://doi.org/10.1016/j.ijsrc.2020.03.006, 2020.

Brodu, N. and Lague, D.: 3D terrestrial lidar data classification of complex natural scenes using a multi-scale dimensionality criterion: Applications in geomorphology, ISPRS J. Photogramm. Remote Sens., 68, 121–134, https://doi.org/10.1016/j.isprsjprs.2012.01.006, 2012.

Browne, G.: Downstream fining and sorting of gravel clasts in the braided rivers of mid-Canterbury, New Zealand, N. Z. Geog., 60, 2–14, https://doi.org/10.1111/j.1745-7939.2004.tb01708.x, 2004.

https://doi.org/10.5194/egusphere-2026-2149
Preprint. Discussion started: 4 May 2026

Buscombe, D., Rubin, D. M., and Warrick, J. A.: A universal approximation of grain size from images of noncohesive sediment, J. Geophys. Res. Earth Surf., 115, 1–17, https://doi.org/10.1029/2009jf001477, 2010.

Carbonneau, P. E., Bergeron, N., and Lane, S. N.: Automated grain size measurements from airborne remote sensing for long profile measurements of fluvial grain sizes, Water Resour. Res., 41, 1–9, https://doi.org/10.1029/2005WR003994, 2005.

Carson, M. A.: Observations on the Meandering-Braided River Transition, The Canterbury Plains, New Zealand: Part Two, N. Z. Geog., 40, 89–99, https://doi.org/10.1111/j.1745-7939.1984.tb01044.x, 1984.

Chapuis, R. P.: Fitting models for a grain size distribution: a review, Bull. Eng. Geol. Environ., 82, https://doi.org/10.1007/s10064-023-03444-5, 2023.

Chavarrías, V., Stecca, G., and Labeur, R. J.: A Well-posed Model for Mixed-Sediment River Morphodynamics, in: E3S Web of Conferences, https://doi.org/10.1051/e3sconf/20184005060, 2018.

Cui, Y.: The unified gravel-sand (TUGS) model: Simulating sediment transport and gravel/sand grain size distributions in gravel-bedded rivers, Water Resour. Res., 43, 1–16, https://doi.org/10.1029/2006WR005330, 2007.

Curran, J. C. and Wilcock, P. R.: Effect of Sand Supply on Transport Rates in a Gravel-Bed Channel, J. Hydraul. Eng., 131, 961–967, https://doi.org/10.1061/(ASCE)0733-9429(2005)131:11(961), 2005.

Dean, D. J. and Schmidt, J. C.: The role of feedback mechanisms in historic channel changes of the lower Rio Grande in the Big Bend region, Geomorphology, 126, 333–349, https://doi.org/10.1016/j.geomorph.2010.03.009, 2011.

Deltares: Delft3d Flexible Mesh Suite, https://www.deltares.nl/en/software-and-data/products/delft3d-flexible-mesh-suite, 2021.

Dudill, A., Frey, P., and Church, M.: Infiltration of fine sediment into a coarse mobile bed: a phenomenological study, Earth Surf. Process. Landforms, 42, 1171–1185, https://doi.org/10.1002/esp.4080, 2017.

Dust, D. and Wohl, E.: Conceptual model for complex river responses using an expanded Lane's relation, Geomorphology, 139–140, 109–121, https://doi.org/10.1016/j.geomorph.2011.10.008, 2012.

Ferguson, R.: The missing dimension: Effects of lateral variation on 1-D calculations of fluvial bedload transport, Geomorphology, 56, 1–14, https://doi.org/10.1016/S0169-555X(03)00042-4, 2003.

Ferguson, R. I., Hardy, R. J., Hodge, R. A., Houseago, R. C., Yager, E. M., and Yamasaki, T. N.: Predicting flow resistance in rough-bed rivers from topographic roughness: Review and open questions, Earth Surf. Process. Landforms, 4888–4907, https://doi.org/10.1002/esp.6016, 2024.

Gaeuman, D., Schmidt, J. C., and Wilcock, P. R.: Complex channel responses to changes in stream flow and sediment supply on the lower Duchesne River, Utah, Geomorphology, 64, 185–206, https://doi.org/10.1016/j.geomorph.2004.06.007, 2005.

Gibb, J. G. and Adams, J.: A sediment budget for the east coast between oamaru and banks peninsula, South Island, New Zealand, New Zeal. J. Geol. Geophys., 25, 335–352, https://doi.org/10.1080/00288306.1982.10421497, 1982.

González del Tánago, M., Bejarano, M. D., García de Jalón, D., and Schmidt, J. C.: Biogeomorphic responses to flow regulation and fine sediment supply in Mediterranean streams (the Guadalete River, southern Spain), J. Hydrol., 528, 751–762, https://doi.org/10.1016/j.jhydrol.2015.06.065, 2015.

Grams, P. E. and Wilcock, P. R.: Equilibrium entrainment of fine sediment over a coarse immobile bed, Water Resour. Res., 43, 1–14, https://doi.org/10.1029/2006WR005129, 2007.

Grams, P. E. and Wilcock, P. R.: Transport of fine sediment over a coarse, immobile riverbed, J. Geophys. Res. Earth Surf., 119, 188–211, https://doi.org/10.1002/2013JF002925, 2014.

Haddadchi, A. and Measures, R. J.: Flow and sediment data Impact of mid-range flow abstraction on sand and fine sediment deposition in gravel-bed braided rivers, Mendeley Data, https://doi.org/10.17632/ptss4vtvkj.1, 2025.

Haddadchi, A. and Rose, C. W.: A Physically Based Model of Deposition, Re-Entrainment, and Transport of Fine Sediment in Gravel-Bed Rivers, Water Resour. Res., 58, https://doi.org/10.1029/2021WR031782, 2022.

Healey, M. O.: Investigation of Flood Risk & Erosion Mitigation on the Rangitata River, 1997.

Hicks, D. M., Shankar, U., Mckerchar, A. I., Basher, L., Lynn, I., Page, M., and Jessen, M.: Suspended sediment yields from New Zealand rivers, J. Hydrol. (New Zeal.), 50, 81–142, 2011.

Hicks, D. M., Baynes, E. R. C., Measures, R. J., Stecca, G., Tunnicliffe, J., and Friedrich, H.: Morphodynamic research challenges for braided river environments: Lessons from the iconic case of New Zealand, Earth Surf. Process. Landforms, https://doi.org/10.1002/esp.5014, 2020.

Hodge, R., Brasington, J., and Richards, K. S.: Analysing laser-scanned digital terrain models of gravel bed surfaces: Linking morphology to sediment transport processes and hydraulics, Sedimentology, 56, 2024–2043, https://doi.org/10.1111/j.1365-

https://doi.org/10.5194/egusphere-2026-2149
Preprint. Discussion started: 4 May 2026

3091.2009.01068.x, 2009.

Hoyle, J. T., Kilroy, C., Hicks, D. M., and Brown, L.: The influence of sediment mobility and channel geomorphology on periphyton abundance, Freshw. Biol., 62, 258–273, https://doi.org/10.1111/fwb.12865, 2017.

Javernick, L., Redolfi, M., and Bertoldi, W.: Evaluation of a numerical model's ability to predict bed load transport observed in braided river experiments, Adv. Water Resour., 115, 207–218, https://doi.org/10.1016/j.advwatres.2018.03.012, 2018.

Jowett, I. G. and Boustead, N. C.: Effects of substrate and sedimentation on the abundance of upland bullies (Gobiomorphus breviceps), New Zeal. J. Mar. Freshw. Res., 35, 605–613, https://doi.org/10.1080/00288330.2001.9517026, 2001.

Jowett, I. G. and Milhous, R.: Why rivers get clearer as they flow downstream, Water Atmos., 10, 16–17, 2002.

Kemp, P., Sear, D., Collins, A., Naden, P., and Jones, I.: The impacts of fine sediment on riverine fish, Hydrol. Process., 25, 1800–1821, https://doi.org/10.1002/hyp.7940, 2011.

Kleinhans, M. G. and van Rijn, L. C.: Stochastic Prediction of Sediment Transport in Sand-Gravel Bed Rivers, J. Hydraul. Eng., 128, 412–425, https://doi.org/10.1061/(asce)0733-9429(2002)128:4(412), 2002.

Kuhnle, R. A.: Fluvial transport of sand and gravel mixtures with bimodal size distributions, Sediment. Geol., 85, 17–24, https://doi.org/10.1016/0037-0738(93)90072-D, 1993.

Kuhnle, R. A., Langendoen, E. J., and Wren, D. G.: Prediction of sand transport over immobile gravel from supply limited to capacity conditions, River Flow 2016 Iowa City, USA, July 11-14, 2016, 143, 969–972, https://doi.org/10.1061/(asce)hy.1943-7900.0001292, 2016.

Larsen, S., Vaughan, I. P., and Ormerod, S. J.: Scale-dependent effects of fine sediments on temperate headwater invertebrates, Freshw. Biol., 54, 203–219, https://doi.org/10.1111/j.1365-2427.2008.02093.x, 2009.

Legleiter, C. J. and Harrison, L. R.: Remote Sensing of River Bathymetry: Evaluating a Range of Sensors, Platforms, and Algorithms on the Upper Sacramento River, California, USA, Water Resour. Res., 55, 2142–2169, https://doi.org/10.1029/2018WR023586, 2019.

López, R. and Barragán, J.: López, Raúl Barragán, Javier, J. Hydraul. Eng., 134, 847–851, https://doi.org/10.1061/(ASCE)0733-9429(2008)134:6(847), 2008.

Marchetti, G., Bizzi, S., Belletti, B., Lastoria, B., Comiti, F., and Carbonneau, P. E.: Mapping riverbed sediment size from Sentinel-2 satellite data, Earth Surf. Process. Landforms, https://doi.org/10.1002/ESP.5394, 2022.

Matthaei, C. D., Weller, F., Kelly, D. W., and Townsend, C. R.: Impacts of fine sediment addition to tussock, pasture, dairy and deer farming streams in New Zealand, Freshw. Biol., 51, 2154–2172, https://doi.org/10.1111/j.1365-2427.2006.01643.x, 2006.

McCarron, C. J., Van Landeghem, K. J. J., Baas, J. H., Amoudry, L. O., and Malarkey, J.: The hiding-exposure effect revisited: A method to calculate the mobility of bimodal sediment mixtures, Mar. Geol., 410, 22–31, https://doi.org/10.1016/j.margeo.2018.12.001, 2019.

Measures, R. J.: Gravel bedload supply estimates : Canterbury Plains Rivers, 9 pp., 2013.

Le Minor, M., Davy, P., Howarth, J., and Lague, D.: Multi Grain-Size Total Sediment Load Model Based on the Disequilibrium Length, J. Geophys. Res. Earth Surf., 127, 1–22, https://doi.org/10.1029/2021JF006546, 2022.

Monsalve, A., Segura, C., Hucke, N., and Katz, S.: A bed load transport equation based on the spatial distribution of shear stress-Oak Creek revisited, Earth Surf. Dyn., 8, 825–839, https://doi.org/10.5194/esurf-8-825-2020, 2020.

Monsalve, A. D., Yager, E. M., Turowski, J. M., and Rickenmann, D.: A probabilistic formulation of bed load transport to include spatial variability of flow and surface grain size distributions, Water Resour. Res., 52, 3579–3598, https://doi.org/10.1002/2015WR017694, 2016.

Nicholas, A. P.: Modelling bedload yield in braided gravel bed rivers, Geomorphology, 36, 89–106, https://doi.org/10.1016/S0169-555X(00)00050-7, 2000.

Parker, G.: Surface-based bedload transport relation for gravel rivers, J. Hydraul. Res., 28, 417–436, https://doi.org/10.1080/00221689009499058, 1990.

Parker, G.: Transport of Gravel and Sediment Mixtures, Chapter 3, Sedimentation Engineering, Sediment. Eng. Theor. Meas. Model. Pract., 110, 165–252, 2008.

Raus, D., Moulin, F. Y., and Eiff, O.: The Impact of Coarse-Grain Protrusion on Near-Bed Hydrodynamics, J. Geophys. Res. Earth Surf., 124, 1854–1877, https://doi.org/10.1029/2018JF004751, 2019.

Redolfi, M., Tubino, M., Bertoldi, W., and Brasington, J.: Analysis of reach-scale elevation distribution in braided rivers: Definition of a new morphologic indicator and estimation of mean quantities, Water Resour. Res., 52, 5951–5970,

https://doi.org/10.5194/egusphere-2026-2149
Preprint. Discussion started: 4 May 2026

https://doi.org/:10.1002/ 2015WR017918., 2016.

Redolfi, M., Bertoldi, W., Tubino, M., and Welber, M.: Bed Load Variability and Morphology of Gravel Bed Rivers Subject to Unsteady Flow: A Laboratory Investigation, Water Resour. Res., 54, 842–862, https://doi.org/10.1002/2017WR021143, 2018.

De Rego, K., Lauer, J. W., Eaton, B. C., and Hassan, M.: A decadal-scale numerical model for wandering, cobble-bedded rivers subject to disturbance, Earth Surf. Process. Landforms, 45, 912–927, https://doi.org/10.1002/esp.4784, 2020.

van Rijn, L. C.: Unified View of Sediment Transport by Currents and Waves. I: Initiation of Motion, Bed Roughness, and Bed-Load Transport, J. Hydraul. Eng., 133, 649–667, https://doi.org/10.1061/(ASCE)0733-9429(2007)133:6(649), 2007a.

van Rijn, L. C.: Unified View of Sediment Transport by Currents and Waves. II: Suspended Transport, J. Hydraul. Eng., 133, 668–689, https://doi.org/10.1061/(asce)0733-9429(2007)133:6(668), 2007b.

Rogers, J. M., Brasington, J., and Hoyle, J.: Bed material facies mapping at braided river scale and evidence for trends in fine sediment, Earth Surf. Process. Landforms, 50, 1–26, https://doi.org/10.1002/esp.70012, 2025.

Schubert, J. E., Monsen, W. W., and Sanders, B. F.: Metric-resolution 2D River Modeling at the Macroscale: Computational methods and applications in a Braided River, Front. Earth Sci., 3, 1–22, https://doi.org/10.3389/feart.2015.00074, 2015.

Singh, U., Crosato, A., Giri, S., and Hicks, D. M.: Sediment heterogeneity and mobility in the morphodynamic modelling of gravel-bed braided rivers, Adv. Water Resour., 104, 127–144, https://doi.org/10.1016/j.advwatres.2017.02.005, 2017.

Smith, H. E. J., Monsalve, A. D., Turowski, J. M., Rickenmann, D., and Yager, E. M.: Controls of local grain size distribution, bed structure and flow conditions on sediment mobility, Earth Surf. Process. Landforms, 48, 1990–2004, https://doi.org/10.1002/esp.5599, 2023.

Stecca, G., Measures, R. J., and Hicks, D. M.: A framework for the analysis of noncohesive bank erosion algorithms in morphodynamic modeling, Water Resour. Res., 53, 6663–6686, https://doi.org/10.1002/2017WR020756, 2017.

Stecca, G., Fedrizzi, D., Measures, R. J., Hicks, D. M., Hoyle, J., and Zolezzi, G.: Development of a numerical model for braided river morphology and vegetation evolution with application to the Lower Waitaki River (Aotearoa - New Zealand), Adv. Water Resour., 166, 104236, https://doi.org/10.1016/j.advwatres.2022.104236, 2022.

Sun, J., Lin, B., and Yang, H.: Development and application of a braided river model with non-uniform sediment transport, Adv. Water Resour., 81, 62–74, https://doi.org/10.1016/j.advwatres.2014.12.012, 2015.

Török, G. T., Józsa, J., and Baranya, S.: Validation of a novel, shear Reynolds number based bed load transport calculation method for mixed sediments against field measurements, Water (Switzerland), 11, 1–20, https://doi.org/10.3390/w11102051, 2019.

Török, G. T., Józsa, J., and Baranya, S.: A novel sediment transport calculation method-based 3d cfd model investigation of a critical danube reach, Polish J. Environ. Stud., 29, 2889–2899, https://doi.org/10.15244/pjoes/111877, 2020.

Trevisson, M. and Eiff, O.: Fine-Sediment Erosion and Sediment-Ribbon Morphodynamics in Coarse-Grained Immobile Beds, Water Resour. Res., 58, https://doi.org/10.1029/2021WR031837, 2022.

Vericat, D., Batalla, R. J., and Gibbins, C. N.: Sediment entrainment and depletion from patches of fine material in a gravel-bed river, Water Resour. Res., 44, 1–15, https://doi.org/10.1029/2008WR007028, 2008.

Wainwright, J., Parsons, A. J., Cooper, J. R., Gao, P., Gillies, J. A., Mao, L., Orford, J. D., and Knight, P. G.: The concept of transport capacity in geomorphology, Rev. Geophys., 53, 1155–1202, https://doi.org/10.1002/2014RG000474, 2015.

Weidner, L., Walton, G., and Krajnovich, A.: Classifying rock slope materials in photogrammetric point clouds using robust color and geometric features, ISPRS J. Photogramm. Remote Sens., 176, 15–29, https://doi.org/10.1016/j.isprsjprs.2021.04.001, 2021.

Welber, M., Bertoldi, W., and Tubino, M.: The response of braided planform configuration to flow variations, bed reworking and vegetation: The case of the Tagliamento River, Italy, Earth Surf. Process. Landforms, 37, 572–582, https://doi.org/10.1002/esp.3196, 2012.

Wilcock, P. R. and Crowe, J. C.: Surface-based Transport Model for Mixed-Size Sediment, 129, 120–128, 2003.

Williams, R. D., Brasington, J., Hicks, D. M., Measures, R. J., Rennie, C. D., and Vericat, D.: Hydraulic validation of two-dimensional simulations of braided river flow with spatially continuous aDcp data, Water Resour. Res., 49, 5183–5205, https://doi.org/10.1002/wrcr.20391, 2013.

Williams, R. D., Brasington, J., Vericat, D., and Hicks, D. M.: Hyperscale terrain modelling of braided rivers: fusing mobile terrestrial laser scanning and optical bathymetric mapping, Earth Surf. Process. Landforms, 39, 167–183, https://doi.org/10.1002/esp.3437, 2014.

https://doi.org/10.5194/egusphere-2026-2149
Preprint. Discussion started: 4 May 2026

Williams, R. D., Rennie, C. D., Brasington, J., Hicks, D. M., and Vericat, D.: Linking the spatial distribution of bed load transport to morphological change during high-flow events in a shallow braided river, J. Geophys. Res. F Earth Surf., 120, 604–622, https://doi.org/10.1002/2014JF003346, 2015.

Williams, R. D., Measures, R. J., Hicks, D. M., and Brasington, J.: Assessment of a numerical model to reproduce event-scale erosion and deposition distributions in a braided river, Water Resour. Res., 52, 6621–6642, https://doi.org/10.1002/2015WR018491, 2016.

Williams, R. D., Lamy, M. Lou, Maniatis, G., and Stott, E.: Three-dimensional reconstruction of fluvial surface sedimentology and topography using personal mobile laser scanning, Earth Surf. Process. Landforms, 45, 251–261, https://doi.org/10.1002/esp.4747, 2020.

Willmott, C. J.: ON THE VALIDATION OF MODELS, Phys. Geogr., 2, 184–194, https://doi.org/10.1080/02723646.1981.10642213, 1981.

Wolman, M. G. and Miller, J. P.: Magnitude and Frequency of Forces in Geomorphic Processes, J. Geol., 68, 54–74, 1960.

Woodget, A. S. and Austrums, R.: Subaerial gravel size measurement using topographic data derived from a UAV-SfM approach, Earth Surf. Process. Landforms, 42, 1434–1443, https://doi.org/10.1002/esp.4139, 2017.

Wren, D. G., Kuhnle, R. A., Langendoen, E. J., and Rigby, J. R.: Turbulent Flow and Sand Transport over a Cobble Bed in a Laboratory Flume, J. Hydraul. Eng., 140, 1–12, https://doi.org/10.1061/(asce)hy.1943-7900.0000838, 2014.